Textures of Peritectic Crystals as Guides to Reactive Minerals in Magmatic Systems: New Insights from Melting Experiments

Saskia Erdmann, Bruno Scaillet, D.A. Kellett

Textures of peritectic crystals as guides to reactive minerals in magmatic systems:

New insights from melting experiments

S. Erdmann[1], B. Scaillet[1], D. A. Kellett[2]

[1] Centre National de la Recherche Scientifique, Institut des Sciences de la Terre d'Orléans,

Université d'Orléans, Université François Rabelais Tours, 45071 France

[2] Department of Earth Science, University of California, Santa Barbara, 93106-3060 USA

Corresponding author: serdmann@dal.ca

Keywords: Crystal cluster; crystal size; olivine; peritectic; reactive minerals

Running title: Peritectic crystals as guides to reactive minerals in igneous rocks

ABSTRACT

Peritectic crystals in igneous rocks may be derived from source or country rocks or may have formed by reactive assimilation of source-inherited solids, primary magmatic minerals during self- or magma mixing, or country-rock xenoliths or xenocrysts. Identifying such peritectic crystals is important for constraining components and textures of igneous rocks and the underlying processes of magmatic evolution. In this paper we demonstrate that peritectic olivine formed in melting experiments crystallizes as clusters of euhedral to subhedral crystals. Olivine replacing orthopyroxene, amphibole, and phlogopite forms crystal clusters with distinct crystals to melt ratio, 2D surface area, grain boundary segmentation, and inclusion relations. In our experiments textures of peritectic crystals are primarily controlled by the stability temperature and decomposition rate of reactive minerals. High-temperature minerals such as orthopyroxene slowly decomposed to form high-density clusters of large crystals with long grain boundary segments. The SiO_2-rich peritectic melt produced favours formation of melt inclusions. Low-temperature minerals such as amphibole and phlogopite rapidly decomposed to form low-density clusters of small crystals with short grain boundary segments. The relatively SiO_2-poor peritectic melt produced results in formation of fewer melt inclusions. Host melt composition, and particularly the concentration of fast-diffusing components, affect cluster assemblages. Cluster density and 2D surface area of peritectic olivine tend to decrease, whilst grain boundary segment length increases with increasing experimental temperature and H_2O content. Using the textural criteria that distinguish olivine formed after different minerals in our melting experiments, we hypothesize that two olivine populations from a basaltic-andesitic lava flow of the Tatara-San Pedro volcanic complex, Chile, may be peritectic crystals formed after amphibole and orthopyroxene. Both amphibole and orthopyroxene are common in xenoliths preserved in some

Tatara-San Pedro lava flows. One notable difference between the experimental and natural olivine crystals is that the natural olivine crystals have 2D surface areas and 2D grain boundary segments up to ~1000 and ~100 times larger, respectively, than those produced in our experiments. We propose that this size difference is primarily controlled by comparatively slow heating and decomposition of reactive crystals and textural coarsening of peritectic crystals during prolonged magma residence in the natural system.

INTRODUCTION

Peritectic crystals have been observed in igneous rocks that are rich in source-inherited solids, record self- or magma mixing, or are contaminated by reactive country rocks (Fig. 1a,b; Couch *et al.*, 2001; Coogan, 2003; Beard *et al.*, 2005; Reubi & Blundy, 2008; France *et al.*, 2009). They form in incongruent reactions of the type primary crystal(s) ± melt1 → melt2 ± peritectic crystal(s) ± fluid, driven by temperature, pressure, redox, or compositional variation. Assemblage, texture, and composition of peritectic crystals may be a guide to their reactive precursor crystals, and thus an important recorder of magmatic reactions and cryptic components of igneous rocks (e.g., Coogan, 2003; Beard *et al.*, 2005; Erdmann et al. 2010). Peritectic crystals have been identified in volcanic and plutonic rocks (e.g., Bédard *et al.*, 2000; Couch *et al.*, 2001; Amma-Miyasaka & Nakagawa, 2002; Erdmann *et al.*, 2009; O'Driscoll *et al.*, 2009; Diaz-Alvarado *et al.*, 2011; Dorais & Tubrett, 2012), but have received little attention in comparison to xenocrysts or antecrysts.

In nature and experiment peritectic crystals form clusters or single euhedral to subhedral grains, with chemical contributions from primary crystals and host melt (Fig. 1c; Brearley & Scarfe, 1986; Bédard *et al.*, 2000; Stevens, *et al.* 2007; Lackey *et al.*, 2011). Inclusions are rare to common in peritectic crystals. They may comprise relics of the reactive mineral, inherited refractory inclusions, and/or components of the host magma (e.g., Clarke, 2007; Dorais & Tubrett, 2012; Lackey *et al.*, 2011). Peritectic crystals in igneous rocks may be easily overlooked, and are potentially under-reported, because they texturally and compositionally resemble clusters of primary magmatic crystals (glomerocrysts) or subhedral phenocrysts.

In this study, we examine textures of peritectic olivine formed in melting experiments. Starting materials for our melting experiments were orthopyroxene leuconorite (LN) and

amphibole-phlogopite melanorite (MN) rocks of the Tatara San Pedro Complex. These materials were selected because they are important reactive contaminants in TSP lavas (Dungan *et al.*, 2001; Costa *et al.*, 2002) that produced abundant peritectic crystals in contamination experiments (Erdmann *et al.*, 2010). The results of our experiments thus best compare to peritectic crystals formed during partial melting in source or country rocks prior to the entrainment in magmas. By comparing our new results to earlier contamination experiments (Erdmann *et al.*, 2010), in which peritectic crystals formed after contaminants immersed in a partially crystallized dacite, we examine effects of host melt composition on assemblages and growth textures of peritectic crystals. We further present textural data for two presumably peritectic olivine types from a basaltic-andesitic lava flow of the Tatara-San Pedro complex of the Southern volcanic zone, Chilean Andes.

We show that experimental decomposition of orthopyroxene, amphibole, and phlogopite produces clusters of peritectic olivine that differ in grain size, grain shape, and crystal-to-melt ratio. We anticipate that future textural analysis of peritectic crystals in igneous rocks will add a subset of information on open-system evolution that is as yet largely untapped. However, further analyses of experimental and natural samples are needed to (i) better constrain textural criteria for identifying peritectic crystals; (ii) to determine effects such as crystallization rate and dynamic conditions on textures of peritectic crystals; and (iii) to devise criteria that unambiguously distinguish between peritectic crystal clusters and magmatic glomerocrysts.

METHODS AND DATA

Olivine from TSP lavas

Olivine populations in TSP lavas are texturally and compositionally diverse, including primary magmatic micro- and macro-crystals, xenocrysts derived from partially crystalline plutonic roots, and peritectic crystals (Dungan & Davidson, 2004; Costa & Dungan, 2005; Erdmann *et al.*, 2010). Here, we examine two texturally distinct types of presumably peritectic olivine from a basaltic-andesite of the middle Estero Molino sequence of the TSP complex (for details of the TSP units see Dungan *et al.*, 2001). Peritectic crystals and xenocrysts are large compared to primary magmatic crystals. They also show void- and mineral-filled embayments and inclusions that are interpreted as melt-film pseudomorphs formed during partial assimilation (Dungan & Davidson, 2004). Peritectic crystals are largely undeformed, whereas xenocrysts commonly show subsolidus deformation features, such as healed micro-fractures and subgrains (Dungan & Davidson, 2004; Costa & Dungan, 2005).

Experimental starting materials

Starting materials for our melting experiments were powders and cores of MN and LN (Fig. 2; Table 1). Major constituents of the MN are largely unzoned plagioclase (predominantly $\sim An_{80}$), amphibole oikocrysts ($X_{Mg} \sim 77$), orthopyroxene oikocrysts ($\sim En_{78}$, Fs_{20}, Ws_2; $X_{Mg} \sim 80$), phlogopite ($X_{Mg} \sim 80$), olivine ($\sim Fo_{78}$) with partial iddingsite rims, and Fe-Ti oxides (Fig. 2a; Table 1,2). Major constituents of the LN are largely unzoned plagioclase (predominantly $\sim An_{53}$), orthopyroxene ($\sim En_{65}$, Fs_{33}, Ws_2; $X_{Mg} \sim 66$), clinopyroxene ($\sim En_{44}$, Fs_{16}, Ws_{40}; $X_{Mg} \sim 74$) with oxide exsolutions, and Fe-Ti oxides (Fig. 2b; Table 1,2).

The coarse-grained LN and MN rocks were crushed to a powder of ≤ 170 μm that consists of crystal fragments and few micro-rock fragments. Powders were homogenized in an agate

mortar to maximize homogeneity of starting materials. Although using these rock powders caused compositional variations between charges it was essential to mimic textural characteristics of natural reactive assimilation. Rock cores used in two experiments are not intended to be representative of the bulk starting material, but were employed to characterize assemblages and crystal textures in a spatial context.

Experimental techniques

A total of 26 experiments were carried out with LN and MN starting materials, using two strategies: (i) most experiments were conducted with rock powders of ≤170 μm; and (ii) two experiments (LN-13c and MN-13c) employed ~8 mm long, ~4 mm diameter drilled rock cores (Table 3). To examine products of partial melting over a large range of temperature and H_2O content, and at redox conditions typical for arc magmas (e.g., Behrens & Gaillard, 2006), experiments with rock powders were conducted between 1000 and 1150 °C, and ~0.5 to 9.6 wt% deionized, ultrafiltered H_2O added to the charges, at a constant pressure of ~200 MPa, and average fO_2 of NNO+0.7. The two experiments with rock cores were performed at equivalent pressure and fO_2 conditions and (i) 1043 °C and ~4.3 wt% H_2O added (LN-13c), and (ii) 1150 °C and ~1.5 wt% H_2O added (MN-13c). One experiment (MN-13c) was run for only ~2 h. All other experiments were run for ~21-25 h. These short run durations were chosen in order to preserve prograde reaction textures. As an intended result, run products did not achieve equilibrium.

Gold capsules were used as sample containers for ≤1043 °C experiments and $Au_{80}Pd_{20}$ capsules were used for ≥1085 °C experiment. Experiments were conducted within internally-heated pressure vessel at the ISTO-CNRS Orléans. Pressure was obtained by sequential loading of a mixture of Ar and H_2 gas at room temperature (cf., Scaillet *et al.*, 1995). Charges were then

heated at a rate of ~10-15 °C/min from room temperature to ~40 °C below the experimental temperature. Final heating to the experimental temperature was performed at ~2-4 °C/min to restrict overstepping of set point temperatures to ≤5 °C for ≤10 min. Cooling of the experimental charges was achieved by drop quench. Experimental $f\mathrm{H}_2$ was recorded using Ni–Pd–NiO solid sensors; experimental $f\mathrm{O}_2$ was calculated from these sensors using the calibration of Pownceby & O'Neill (1994).

Textural analysis of run products and TSP olivine

Experimental run products were mounted in epoxy resin and polished. Back-scattered electron (BSE) images were acquired at the ISTO-CNRS, Orléans, and at Dalhousie University, Halifax. In our description of the experimental run products we distinguish between restitic, newly crystallized, and peritectic crystals. Table 3 reports run products and conditions of all experiments. Figure 3 summarizes characteristic textures of run products and selected natural TSP olivine types. Crystals of the experimental starting materials (LN or MN) are classified as restitic (Ol1, Opx1 etc.). They are <170 μm in diameter, zoned to unzoned, and commonly exhibit glass along micro-fractures. Grain shapes range from subhedral to sub-angular and sub-rounded. Newly-formed crystals are classified as recrystallized, cotectic, or peritectic. Plagioclase of the starting material that dissolved and epitactically reprecipitated is referred to as recrystallized. We interpret single, subhedral to euhedral crystals <10 μm in size as cotectic. Alternatively, we assign a peritectic origin to crystal clusters with randomly-oriented individual crystals that are <30 μm long, zoned to unzoned, and subhedral to euhedral (cf. Erdmann *et al.*, 2010). Modal abundances of experimental run products were constrained by mass-balance. The

abundance of restitic versus peritectic olivine and restitic, anorthite-poor plagioclase versus recrystallized, anorthite-rich plagioclase was estimated using BSE images.

Texturally-variable peritectic olivine crystals were visually sub-classified into Ol2a to Ol2d for the melting experiments and Type-1 Ol and Type-2 Ol for the natural TSP samples. The subtypes were qualitatively distinguished on the basis of (i) inclusion relations; (ii) olivine crystal size and grain boundary segmentation; and (iii) the ratio of olivine to interstitial glass (referred to as cluster density) (Fig. 4). For the pre-classified olivine types we then quantified 2D surface area, 2D grain boundary segment (GBS) length, and 2D cluster density to provide data on the most distinctive textural features of the olivine crystals in our experiments. Moreover, crystal size and grain shape or grain boundary segmentation are among the most commonly used textural features to qualitatively or quantitatively detect various crystal populations in igneous rocks, for which our data sets may serve as a useful reference.

For the textural analyses of run products (Fig. 5a-c), outlines of peritectic crystals were drawn by hand on BSE images (Fig. 5b). Crystals intersecting edges of images were discarded. Drawings were processed using the SCION image software to calculate 2D surface area and 2D cluster density (2D surface area of crystals/cluster glass) (Fig. 5c). The 2D grain boundary segment (GBS) length, measured as length of grain boundary outlines bounded by inflection points, was determined using CorelDRAW (Fig. 5b). For each sample and peritectic cluster type we analyzed three to six individual clusters. We present 2D surface area and cluster density data for the first 100 crystals measured using the SCION software and analyses of 250 GBSs measured on up to 40 of these crystals, where all segments of individual crystals were analyzed. For 2D surface area and GBS length, we defined frequency peaks as comprising ≥70% of the analyzed population. Three-dimensional crystal size was not calculated, because some peritectic

crystals have spherical to highly anhedral shape. We estimate that the measurement error for GBS length is up to ±2 um. In addition to average data acquired for four representative experiments (LN-1, LN-2, LN-8, and MN-8), we present analyses of 2D surface area and 2D GBS length for six individual olivine clusters of one sample (LN-8) to estimate variance between clusters. Standard errors for 2D surface area and 2D GBS length are ≤5 % and ≤2 % of the population range. Calculated cluster density is semi-quantitative, because the area of cluster glass is difficult to determine (i.e. original crystal outlines are unknown).

For the textural analyses of natural olivine in TSP samples, we characterized two olivine types from three thin sections of two samples. We quantified 2D cluster density (where applicable), 2D surface area, and GBS length (Fig. 5d-f). We extrapolated GBSs across olivine-matrix intergrowths and ≤50 μm wide embayments to reduce effects of late-stage crystallization or resorption on our data set (Fig. 5e). Peritectic crystals were identified and selected on the basis of: (i) large surface area (relative to primary magmatic crystals); (ii) presence of multiphase inclusions and embayments; (iii) absence of healed micro-fractures or subgrains; (iv) spatial association with xenocrysts; and/or (v) association in clusters (cf. Erdmann *et al.*, 2010)

Bulk and mineral compositions

Bulk composition of the starting materials was analyzed using a Phillip's PW2400 X-ray spectrometer at the Regional Geochemical Centre of Saint Mary's University, Halifax. For experimental run products, mineral and glass compositions were determined using JEOL 8200 electron microprobes at Dalhousie University and the University of Lausanne. Mineral analyses were performed at 15 keV and 15 nA, with a 2–3 μm spot size, and 40 s counting times. Glass analyses employed 15 keV and 10 nA, with a 10 μm spot size, and 40 s counting times, and were

corrected relative to hydrous glass standards of Scaillet & Evans (1999). Decreasing core-rim X_{Mg} [Mg/(Mg+Fe)*100] and X_{Ca} [Ca/(Ca+Na)*100] are described as normal zoning, and opposite trends as reverse zoning. Mineral abbreviations follow recommendations by Whitney & Evans (2010), and are otherwise defined in respective figure and table captions.

We present mineral-melt partition coefficients as $(Fe/Mg)_{Ol}/(Fe/Mg)_{Gl}$ (total Fe as FeO) and $(Ca/Na)_{Pl}/(Ca/Na)_{Gl}$ that were calculated using cores of unzoned olivine and rims of recrystallized plagioclase and average glass compositions. We provide the calculated partition coefficients for comparison, but note that they are disequilibrium values. First, none of the calculated partition coefficients are representative of the starting material compositions, because restitic crystals are present. Second, plagioclase-melt Ca-Na partition coefficients likely reflect local and temporary equilibrium, but not equilibrium throughout the charges (cf. Johannes *et al.*, 1994) This clearly limits the comparison of our compositional data to natural samples, but it is important to note that peritectic and recrystallized minerals formed in natural systems may equally have disequilibrium composition. Third, Fe-Mg partition coefficients are affected by experimental Fe loss from charges. Calculated average Fe loss is -48% in experiments at 1150 °C and -27% in experiments at 1085 °C (Table 3). Iron loss estimates for 1000 and 1043 °C experiments are not available, owing to large analytical uncertainties in mass-balance calculations, but calculated Fe loss was -13% in crystallization experiments performed at equivalent conditions (Erdmann unpublished data). Estimates are variable owing to compositional variation of the starting rock powders and analytical uncertainty. The high degree of Fe loss in our high-temperature experiments limits direct application of our compositional data, but insights gained from our textural analysis remain directly applicable.

RESULTS

Leuconorite partial melting

Leuconorite powder and core melting experiments yield restitic plagioclase, ±clinopyroxene, orthopyroxene, and oxide (combined up to ~46 wt%), recrystallized plagioclase ±oxide (up to ~28 wt%), ±peritectic olivine (up to ~7 wt%), and glass (~32-100%) (Table 3,4; Figs 6a-c, 7a-c). Mineral-glass proportions and glass compositions vary between powder and core experiments, as starting materials of the core experiments did not have average LN composition and larger crystal size favoured metastable preservation of restitic cores. Mineral textures are comparable between run products of powder and core melting experiments as described below (Fig. 7). Restitic crystals are preserved in all charges except one (LN-6), where modal abundance decreases sharply with increasing experimental temperature and H_2O (Fig. 6b,c). Restitic orthopyroxene is present in experiments with ~0.5 wt% H_2O at ≤1085 °C (e.g., Fig. 7b). Crystals are anhedral to sub-rounded, unzoned, and mantled by peritectic olivine. Restitic clinopyroxene is present in experiments at ≤1043 °C (e.g., Figs 7a,c). Crystals lack zoning, and range from sub-angular at low temperature to rounded at high temperature. They commonly contain irregularly-shaped glass inclusions. Restitic oxide crystals are present in experiments at ≤1043 °C and ≤4.3 wt% H_2O (Fig. 7c). They form sub-rounded cores, rimmed by recrystallized, spongy-cellular oxide. Restitic plagioclase is preserved in all run products as textureless cores (Pl1a). Recrystallized plagioclase (Pl1b) forms subhedral to cellular rims (Pl1b) (Fig. 7a,c). Cellular-textured plagioclase predominates and grain boundaries of plagioclase are increasingly sub-rounded in the high-H_2O and high- temperature experiments. Cores of restitic plagioclase (Pl1a) have ~An_{55-50}, equivalent to plagioclase of the starting material. Rims of recrystallized plagioclase (Pl1b) have

~An$_{85-68}$ (Table 4; Fig. 8a). Calculated Ca/Na Partition coefficients between rims of recrystallized plagioclase (Pl1b) and melt vary between ~2.1 and 5.5 (Table 7) in high- and low-H$_2$O experiments, respectively. Equivalent compositional variation has been documented in previous experimental studies (e.g., Sisson & Grove, 1993; Scaillet & Evans, 1999), but our calculated coefficients likely reflect local or temporary rather than charge-wide plagioclase-melt equilibrium (cf. Johannes *et al.*, 1994).

Peritectic olivine (Ol2a) is present in experiments at ≤1085 °C (Fig. 6b,c, 7a-c). Modal abundance decreases from ~7 to 1 wt% with increasing temperature and to a lesser degree with H$_2$O (Table 3). Crystals form clusters enveloped by glass, in which olivine constitutes ~81 to 65 vol% in low- and high-temperature experiments, respectively (Table 5). Individual olivine crystals are euhedral to subhedral. Crystals rimming orthopyroxene have euhedral inner and subhedral outer GBSs (Fig. 7b). Some contain glass or round orthopyroxene inclusions. They have 2D surface area of commonly <1000 μm^2, but up to ~5800 μm^2 large crystals are present in the low-temperature experiments (Table 5; Fig. 9a,c,e). Grain boundary segment length is usually <20 μm long. The mean GBS length increases from ~4.2 to ~6.4 μm with experimental H$_2$O and temperature. The mode of GBS length increases from ~2.5 to ~5.5 μm (Table 5; Fig. 9b,d,f). Characteristic is that frequency peaks for 2D surface area and 2D GBS length are relatively broad (~900 μm^2 and 5 μm wide, respectively). The 2-D surface area and cluster density show some and the 2D GBS length shows considerable variation between individual clusters of one sample. The six individual clusters analyzed for LN-8 have cluster densities between ~60 and 70% (sample average 65%), a mean 2-D surface area of ~247-293 (sample average 264 μm^2), and a mean 2-D GBS length of ~6.2-8.0 (average 6.4). Ol2a crystals are unzoned to weakly reversely zoned and have ~Fo$_{81}$ in high-temperature experiments and Fo$_{≤70}$ in low-temperature experiments

(Table 6, Fig. 8b). Calculated olivine-melt Fe/Mg partition coefficients vary between ~0.39 and 0.27 (Table 7), but are high as a result of Fe loss and not representative for the investigated bulk composition and assemblages.

Glasses produced by LN melting are basaltic-andesitic, calcalkalic to calcic, and magnesian (Table 7). Contents of SiO_2, (~50-54 wt%) Na_2O (~4-5 wt%), K_2O (~4-5 wt%), and FeO (~3-9 wt%) decrease, and Al_2O_3 (~15-21 wt%) and CaO (~7-9 wt%) increase with temperature and H_2O content (Fig. 8c,d).

Melanorite partial melting

Melanorite powder and core melting experiments yield restitic plagioclase and olivine, ±orthopyroxene and oxides (combined ~7 to 57 wt%), recrystallized plagioclase ±oxides (up to ~33 wt%), peritectic olivine (~4-14 wt%), ±cotectic spinel (<1 wt%), and glass (~16-71 wt%) (Table 3,4; Figs 6e,f, 7d-i). Mineral-glass proportions and glass compositions vary between powder and core experiments, but run products have comparable textures. Restitic oxide crystals occur in experiments at ≤1043 °C. They typically display solid cores <50 μm in diameter and up to ~50 μm wide, recrystallized vermicular rims. Restitic orthopyroxene is present in experiments with 0.5 wt% H_2O at ≤1085 °C, and in the ~2 h experiment MN-13c (Fig. 7h). Crystals are subhedral to anhedral, unzoned, and mantled by peritectic olivine. Restitic olivine and plagioclase are present in all run products. Olivine exhibits gradual core-rim zoning (Fig. 7d-i), and commonly subhedral to euhedral protrusions. Some crystals contain melt inclusions or nanopores (i.e. pores that are probably fluid-filled; e.g., Fig. 7h). Crystal cores have ~Fo_{81-78} composition, equivalent to olivine of the starting material (Table 2). They show normal zoning in experiments at ≤1043 °C and ≤2.7 wt% H_2O (Fig. 7d,e), and reverse zoning in experiments at ≥1043 °C and

≥4.8 wt% H_2O (Fig. 7f-i). Rims have ~Fo_{91} composition in high-temperature experiments and ~Fo_{74} in low- temperature experiments (Fig. 8b). Plagioclase (Pl1a) is angular with <5 μm-thick irregular, recrystallized An-rich rims (Pl1b) in low-temperature, low-H_2O experiments, and subhedral to anhedral with recrystallized, cellular-textures Pl1b rims in high-temperature, high-H_2O experiments. Restitic Pl1a has ~An_{82-77}, equivalent to plagioclase of the starting material. Recrystallized Pl1b has ~An_{83-93} (Table 4; Fig. 8a). Calculated Ca/Na partition coefficients for rims of recrystallized plagioclase (Pl1b) vary between ~4.7 and 9.4 (Table 7) in low- and high-H_2O experiments. They are at the high end of published values (e.g., Sisson & Groove 1993). As for recrystallized plagioclase of the LN melting experiments we interpret the plagioclase-melt partition coefficients as disequilibrium values. Euhedral to subhedral and skeletal cotectic spinel crystals <10 μm in diameter are dispersed throughout charges of ≥1085 °C experiments. They have ferroan chromian spinel composition (~$Al_{1.9}$, $Cr_{0.1}$, $Mg_{0.8}$, $Fe^{2+}_{0.2}$).

Peritectic olivine is present in run products of all experiments (Table 3). As in the LN melting experiments, crystals form clusters enveloped by glass. However, in the MN melting experiments three types of peritectic olivine clusters (Ol2b-d) are present, characterized by different 2D cluster density, 2D crystal surface area, 2D GBS length, or inclusion relations (Fig. 4b-d). As with peritectic olivine of the LN melting experiments, individual crystals are euhedral to anhedral. Cluster density decreases with increasing temperature. Mean 2D surface area decreases with temperature. Mean 2D GBS length increases with H_2O, and less so with temperature (Table 5). Crystals are unzoned or show weak reverse zoning. They have ~Fo_{91} in high-temperature and ~Fo_{74} in low-temperature experiments (Table 6). Major-element compositions of all three cluster types are indistinguishable where tested. Calculated olivine-melt Fe/Mg partition coefficients vary between ~0.23 and 0.39 in low- and high-temperature

experiments, respectively (Table 7). As a result of Fe loss during the experiments, the calculated olivine-melt partition coefficients are high and not representative for the investigated bulk composition and assemblages. In the following, we describe peritectic olivine crystals formed in MN-8 and compare their textures to those of Ol2a formed in LN-8 (Fig. 4, 9e,f, 10; experiments were run at 1085 °C, ~1.5 wt% H_2O). We focus on these experiments because they approximate temperature-H_2O conditions that have been estimated for contamination and partial crystallization of some TSP magmas (Costa *et al.*, 2004; Costa & Dungan, 2005).

The predominant cluster type of the MN melting experiments, Ol2b, has a density of ~60 vol% (Table 5; Fig. 4b). Glass inclusions in crystals are rare. While most crystals have 2D surface areas <300 μm^2, O12b clusters contain large crystals with up to ~1800 μm^2 (Fig. 10a). The mode of 2D GBS length lies at ~2.5 μm, the mean is ~3.7 μm, and the maximum GBS length is ~13 μm (Fig. 10b). Frequency peaks for 2D surface area and 2D GBS length are ~200 μm^2 and 4 μm wide. Peritectic olivine classified as Ol2c has a cluster density of ~68 vol% (Fig. 4c). The Ol2c crystals mantle restitic orthopyroxene in low-H_2O experiments and in MN-13c (e.g., Fig. 7f). Glass inclusions are typically present, and crystals of low-temperature experiments also contain restitic orthopyroxene inclusions <10 μm in diameter. The maximum 2D surface area is ~4600 μm^2, with >60% of all crystals >300 μm^2 in size (Fig. 10c). The mode of 2D GBS length lies at ~4.5 μm, the mean is ~6.1 μm, and the maximum GBS length is ~23 μm (Fig. 10d). Frequency peaks for 2D surface area and 2D GBS length are ~500 μm^2 and 5 μm wide. Crystals classified as peritectic Ol2d form clusters with a density of ~32 vol% (Fig. 3d). The 2D surface area is ≤300 μm^2 (Fig. 10e). The mode of 2D GBS length lies at ~2.5 μm, the mean is ~3.7 μm, and the maximum GBS length is ~21 μm (Fig. 10f). Frequency peaks for 2D surface area and 2D GBS length are <100 μm^2 and 4 μm wide. In comparison, Ol2a of LN-8 has a cluster density of

~65 vol%, intermediate between the cluster densities of Ol2c (~68%) and Ol2b (~60%). The 2D surface area of Ol2a is $\leq$1000 μm^2, and thus larger than for Ol2d ($\leq$300 μm^2), but smaller than for Ol2b ($\leq$1800 μm^2) and Ol2c ($\leq$4600 μm^2). Mode, mean, and maximum length of 2D GBS length are ~5.5 μm, ~6.4 μm, and ~26 μm, and hence are closest to those of Ol2c (~4.5 μm, 6.1 μm, and 23 μm). Variation in 2D surface area, 2D GBS length, and density of individual olivine clusters in one sample are on the same order as those of clusters C1 to C6 of LN-8. One or more of the textural features of peritectic olivine is nevertheless distinct from those of the other two olivine types. For example, Ol2c always has a larger average 2D surface area than Ol2b and Ol2d, and a larger cluster density than Ol2d.

Glasses are predominantly basaltic to andesitic, calcalkalic, and magnesian. Their SiO_2 (~47-55 wt%), Na_2O (~3-4 wt%), K_2O (~0.5-1.5 wt%), and FeO (~4-10 wt%) levels decrease, and Al_2O_3 (~17-22 wt%) and CaO (~7-11 wt%) levels increase with experimental temperature and H_2O content (Fig. 8c,d). Because of short run durations and experimental Fe loss, glasses have non-equilibrium composition.

Olivine in TSP lavas

We texturally analyzed two olivine types in TSP lavas of the middle Estero Molino sequence, because we suspected that they have a peritectic origin based on their textural similarity to peritectic olivine formed in our melting and previous contamination experiments. The two olivine types form crystal clusters (Type-1 Ol) and crystals with irregular shape (Type-2 Ol) that resemble peritectic crystals in the present melting and earlier contamination experiments (Erdmann *et al.*, 2010). Both olivine types lack ductile deformation features. Type-2 olivine commonly shows features that are interpreted as crystallized, exotic melt film pseudomorphs

formed by partial melting of contaminants and that contain re-grown orthopyroxene, phlogopite, and sodic feldspar (cf., Dungan & Davidson, 2004; Costa & Dungan, 2005). Moreover, reactive minerals including amphibole, phlogopite, and orthopyroxene are common in xenoliths enclosed in dacitic TSP lavas (Costa *et al.*, 2002).

In our sample set only one Type-1 olivine cluster is present (Fig. 11a). The analyzed cluster has a density of ~60-70 vol%; individual crystals have euhedral to sub-rounded shapes. The mode of 2D GBS length is ~0.10-0.15 mm, the mean is ~0.17 mm, and the maximum GBS length is ~0.7 mm (Fig. 11b). The mean 2D surface area is ~0.25 mm^2, but ranges up to ~1.2 mm^2 in size (Fig. 11c). Frequency peaks for 2D GBS length and 2D surface area are <0.3 mm and ~0.2 mm^2 wide (Fig. 11b,c). Crystals are inclusion-poor, but contain rare oxide or silicate inclusions <100 µm in size.

Another olivine type, referred to as Type-2 olivine, typically forms single crystals and rare clusters comprising few crystals (Fig.11d). Type-2 olivine is common in our MEMS samples, but given the large crystal size of Type-2 olivine few crystals are present in our three thin sections. The Type-2 crystals have euhedral to anhedral, but predominantly subhedral shapes that commonly exhibit several lobes. The mode of 2D GBS length is ~0.25-0.30 mm, the mean is ~0.33 mm, and the maximum GBS length is ~1.2 mm (Fig. 11e). The 2D surface area ranges up to ~2.5 mm^2, with a mean size of ~1.1 mm^2 (Fig. 11f). Frequency peaks for 2D GBS length and 2D surface area are ~0.3 mm and ~0.9 mm^2 wide (Fig. 11e,f). Most crystals show embayments and inclusions that are up to ~500 µm long and <150 µm wide (i.e. crystallized melt inclusions and melt films), filled by multiple minerals±void space. Small Type-2 crystals, however, may have been inadvertently excluded as they are difficult to distinguish from apparent magmatic phenocrysts.

Type-1 and Type-2 olivine crystals have thus 2D surface areas and GBS lengths that are up to ~1000 and ~100 times larger, respectively, than the experimentally produced peritectic olivine (Table 5). However, distribution of crystallized melt inclusions and melt films, patterns of 2D surface area and GBS length of Type-1 and Type-2 olivine resemble those of Ol2b formed after amphibole and Ol2a and Ol2c formed after orthopyroxene, respectively.

DISCUSSION

Experimental conditions

Before we proceed to discuss our data, we consider potential limitations related to the experimental conditions. The use of starting rock powders enabled us to produce textures that presumably closely mimic those formed during natural partial melting, but in consequence introduced some compositional and mineralogical variation. Our melting experiments, as opposed to contamination experiments, mimic partial melting of rocks with no direct contact to magmas. Constant experimental heat supply during experiments dictates that they are most applicable to natural systems in which heat required for assimilation is effectively buffered. Fast experimental heating best simulates melting of rocks that reach magmatic temperature within minutes to hours. Short run durations have resulted in partial survival of refractory minerals, limited textural annealing of run products, and partial compositional disequilibrium between minerals and glasses. With longer run times, mineral decomposition and diffusive reequilibration between crystals and melt would have continued. The results of our experiments are thus best compared to natural samples that experienced rapid partial melting followed by quenching, such as xenolith cores entrained in rapidly ascending magmas.

We note that the calculated Fe-Mg and Ca-Na partition coefficients likely vary as a result of non-quantified compositional variation between charges. Because of incomplete partial melting and re-equilibration between minerals and melt, calculated partition coefficients are not representative for the bulk starting material. Plagioclase-melt partition coefficients likely represent local and temporary equilibrium during melting, andt charge-wide equilibrium values. Average experimental Fe loss of $\leq13\%$ and up to ~48% decreased FeO and increased X_{Mg} in our run products. As a result, calculated Fe-Mg partition coefficients are lower than equilibrium values. Cotectic spinel in ≥1085 °C experiments likely formed as a result of Fe loss, the stability of restitic Fe-Ti oxides was reduced, and orthopyroxene and clinopyroxene dissolution may have been increased. Without Fe loss, we estimate that peritectic olivine in LN experiments would have ~Fo_{77-62} (instead of ~Fo_{81-63}), and that rims of restitic olivine and peritectic olivine in MN experiments would have ~Fo_{87-73} composition (instead of ~Fo_{91-74}).

Reactive and restitic minerals

Partial melting of LN and MN consumed several reactive rock-forming minerals, including amphibole and phlogopite, that are entirely lacking from run products of MN melting experiments. Orthopyroxene has reacted out in experiments with >0.5 wt% H_2O. The olivine-rims on restitic orthopyroxene crystals indicate that they may not survive with run times longer than ~25 h at the investigated temperature-H_2O conditions. Small sub-rounded cores and recrystallized vermicular rims of restitic oxide similarly indicate that those crystals were undergoing decomposition, and have limited long-term survival. Restitic clinopyroxene is present in ≤1043 °C experiments, but rapidly decomposed at higher temperatures. Plagioclase (Pl1a) is reactive, particularly in high-H_2O and high-T experiments. Recrystallization to Pl1b slows the

dissolution of restitic cores, particularly in low-temperature, low-H_2O experiments, in which Pl1b forms subhedral rims on Pl1a. Reaction rims of this type may be common on partially preserved reactive xenocrysts and antecrysts, followed by layers of cotectic overgrowth.

Olivine is relatively refractory, producing restitic crystals in all MN experiments (Table 3). We interpret zones with abundant glass inclusions and nanopores as the recrystallization products of iddingsite (Id $\rightarrow$ Ol $\pm$ L $\pm$ F; F=fluid). Low- and high-forsterite overgrowths on restitic cores in low- and high-temperature experiments, respectively, efficiently protect them from dissolution. Partial survival of restitic olivine during reactive assimilation is thus likely regardless of its composition, as long as olivine is part of the stable assemblage.

Formation of peritectic olivine

Partial melting of LN starting material produces peritectic olivine in all experiments except those at ≥1150 °C or high H_2O content (Table 3). Peritectic Ol2a rims around orthopyroxene and <50 μm orthopyroxene inclusions in some olivine crystals indicate that orthopyroxene melted incongruently (Figs 4a, 7b, 12a,b). Evidence for incongruent decomposition of clinopyroxene is lacking (e.g., Fig. 7a).

Partial melting of MN starting material produces peritectic olivine in all experiments (Table 3). Olivine may have formed after amphibole, orthopyroxene, or phlogopite. Amphibole is most abundant in the starting material, and thus likely to have formed the most abundant Ol2b cluster (Fig. 12c,d). Peritectic Ol2c forms rims on orthopyroxene in low-T experiments, and in the ~2 h melting experiment at 1085 °C and ~1.5 wt% H_2O (Fig. 7h). Few crystals of low-temperature experiments also have orthopyroxene inclusions <10 μm in diameter. Moreover, 2D surface area, GBS length, and cluster density of Ol2c resemble those of Ol2a formed after

orthopyroxene in LN melting experiments (Figs 7a,b, 9e,f, 10c,d). We thus infer that Ol2c formed by orthopyroxene decomposition (Fig. 12e,f), and accordingly that Ol2d formed after phlogopite (Fig. 12g,h).

Peritectic crystals as guides to reactive minerals

Peritectic crystals are important evidence for source- or country-rock-derived components or, reactive primary magmatic minerals. Their trace-element compositions may point towards the replacement of specific precursor minerals (e.g., Bédard & Hébert, 1998), and isotopic compositions may distinguish peritectic crystals formed after solids derived from the source, country rocks, or magmatic crystals (e.g., Lackey *et al.*, 2011). Inclusions in peritectic crystals, such as orthopyroxene in Ol2a and Ol2c may further provide evidence for the minerals replaced by peritectic crystals, but may be rare (e.g., Figs 4, 7). As summarized below, our results show that in addition to trace-element compositions textures of peritectic crystals such as 2D cluster density, surface area, and GBS length may be useful for identifying the minerals replaced by peritectic crystals, and thus magmatic reactions and cryptic source- or country-rock contributions to igneous rocks (Fig. 12). Using textural criteria to define populations or distinguish peritectic crystals of various origins is particularly important for peritectic minerals with fast diffusive re-equilibration such as olivine.

In our run products peritectic crystal cluster density decreases with the stability temperature of the assimilated mineral, from olivine clusters replacing orthopyroxene to those formed by decomposition of amphibole and phlogopite (Fig. 12). High-density peritectic crystal clusters formed by partial melting thus point towards decomposition of high-temperature minerals or low-temperature assimilation, and low-density peritectic crystal clusters to

decomposition of low-temperature minerals or high-temperature assimilation. The 2D surface area and GBS length decreases with the dissolution rate of the assimilated mineral (e.g., Zhang *et al.*, 1989; Edwards & Russell, 1996 for mineral dissolution rates), from those replacing orthopyroxene in MN melting experiments to those replacing phlogopite. Fast dissolution of phlogopite and amphibole formed abundant small olivine crystals (typically <500 μm^2) with predominantly ~2 to <8 μm-long 2D GBSs. Slow dissolution of orthopyroxene formed relatively few, but large olivine crystals (many >500 μm^2) and a large number of 2D GBSs that are >8 μm long. Moreover, olivine nucleation may have been slow in orthopyroxene-derived versus amphibole- and phlogopite-derived partial melt. Glass inclusions are common in Ol2a and Ol2c, rarely present in Ol2b, and lacking in Ol2d. Partial melt produced by orthopyroxene decomposition is relatively SiO_2-rich and viscous compared to partial melt produced by amphibole and phlogopite breakdown, which facilitated the formation of melt inclusions.

In our experiments, cluster density and 2D surface area are the most distinguishing features of peritectic olivine formed after orthopyroxene, amphibole, and phlogopite (Fig. 12). However, flow or gravity settling in natural magmas may spatially separate peritectic crystals or facilitate synneusis, thereby modifying cluster density. Quantifying the distribution of both 2D surface size and 2D GBS length of peritectic crystals may nevertheless be a useful guide to distinguish between peritectic crystals formed after different minerals. For example, olivine crystals formed after amphibole (Ol2b) and orthopyroxene (Ol2a,2c) form small to large crystals in our experiments, but Ol2b has predominantly short GBS segments and Ol2a and Ol2c typically show long GBSs (Fig. 12b,d). Further experiments and studies of natural examples need to examine whether crystal size and GBS length or other textural criteria can be used unambiguously distinguish between peritectic crystals and magmatic glomerocrysts and how

other parameters such as crystallization rate and dynamic conditions affect textures of peritectic crystals. That peritectic crystals formed after different minerals feature variable textures seems logical, as reaction and crystallization kinetics that control crystal textures vary with system composition (i.e. with the composition of the reactive mineral).

Comparison between peritectic crystals in melting and MN contamination experiments

Previously, we described peritectic crystals formed in contamination experiments in which we added ~25 wt% MN contaminant to a partially crystallized, hydrated basaltic andesite glass (Erdmann *et al.*, 2010). Clusters of olivine-plagioclase, olivine-plagioclase-clinopyroxene, and olivine formed, which we interpreted as the peritectic decomposition products of amphibole, amphibole and orthopyroxene, and phlogopite, respectively. The conditions of the contamination experiments compare to those of our melting experiment MN-8 at 1085 °C and ~1.5 wt% H_2O added, in which olivine formed as the only peritectic phase. One possible cause for the differing peritectic crystal assemblages is that we added H_2O to the charges of the melting experiments, but used a hydrated glass in the contamination experiments. In the melting experiments, a H_2O-rich fluid and melt was thus present during initial partial melting, which stabilizes olivine relative to plagioclase and clinopyroxene.

Another possible cause for the different peritectic assemblages formed by partial melting of the MN starting material is that the host melt $CaO\pm Al_2O_3$ contributed to their crystallization. The contamination experiments have glass relatively high in Al_2O_3 and CaO compared with glasses of the melting experiments. However, plagioclase decomposition, which contributed much of the melt CaO and Al_2O_3 in the melting experiments, is slow compared to decomposition of amphibole and phlogopite (e.g., Zhang *et al.*, 1989; Edwards & Russell, 1996). Melt

composition in LN and MN melting experiments during formation of peritectic olivine was thus lower in $CaO\pm Al_2O_3$ than the quenched glass, and may have been too low to have promoted crystallization of peritectic plagioclase or clinopyroxene. On the contrary, CaO and Al_2O_3 of the basaltic-andesitic host in our contamination experiments were readily available for reaction with the decomposing mafic phases.

In our previous contamination experiments (Erdmann *et al.*, 2010), we classified peritectic crystal cluster according to their mineral assemblage, and did not use textural criteria to distinguish different cluster types. We interpreted the most abundant cluster type of olivine-plagioclase (Fig. 13a,c) as the product of amphibole decomposition, because amphibole accounts for most of the assimilated crystals and contains appreciable amounts of CaO and Al_2O_3. For the second most common cluster type of olivine, we inferred phlogopite and iddingsite as the likely precursor minerals. We further proposed that orthopyroxene partially dissolved (i.e. crystals form rounded xenocrysts), but reacted with amphibole to form clusters of olivine-plagioclase-clinopyroxene (Fig. 13b). However, a qualitative comparison of olivine crystal size, grain boundary segmentation, and cluster density reveals two distinct olivine types in our C2 contamination experiment and suggests a re-interpretation of our earlier results. The most common olivine type forms small to large crystals with short GBSs in medium-density clusters that contain An-rich plagioclase (Fig. 13a). Olivine textures and abundance within the clusters compare to those of Ol2b in our melting experiments, which we interpret as the decomposition product of amphibole. Olivine in clusters with plagioclase and clinopyroxene in contact with orthopyroxene (Fig. 13b) have 2D surface area and GBS length comparable to Ol2b, but a lower cluster density. We consider it likely that these clusters formed in a reaction between amphibole and clinopyroxene and that the low olivine cluster density is a result of clinopyroxene formation

(i.e. competition for Fe and Mg). Another olivine type is rare and forms predominantly small crystals with short GBSs in low-density clusters that also contain An-rich plagioclase (Fig. 13c). This olivine type compares to Ol2d of our melting experiments, which we interpret to have formed after phlogopite. Previously, we assumed that all plagioclase-bearing clusters formed by amphibole decomposition and that CaO derived from amphibole was crucial to stabilize plagioclase in the clusters. On the basis of our new data and a much larger set of experiments, we consider it likely that Al_2O_3 of phlogopite (~15.9 wt%) and amphibole (~11.5 wt%) stabilized plagioclase in the clusters, and that the relatively fast-diffusing Ca and Na components were largely derived from the host melt.

In another contamination experiments (C4; Erdmann unpubl. data), which was run together with our contamination experiment C2 (Erdmann *et al.*, 2010) and also employed a partially crystallized basaltic andesitic glass and ~25 wt% MN but ~2.5 wt% H_2O (instead of ~1.5 wt%), olivine formed as the only peritectic phase and orthopyroxene is absent. Again, using surface area, GBS length, and cluster density three different types of olivine are recognizable. Clusters characterized by relatively large crystals with commonly long GBSs, common glass inclusions, and high cluster density that resemble Ol2c are interpreted as the products of orthopyroxene (Fig. 13d, they are absent from C2). Clusters characterized by small to large crystals with short GBSs and medium to high cluster density that resemble Ol2b and are interpreted as the products of amphibole (Fig. 13e). Clusters characterized by small crystals with short GBSs and low cluster density that resemble Ol2d and are interpreted as the products of phlogopite (Fig. 13f).

A set of textural features – i.e. the range in crystal size, GBS length, and cluster density – thus permit the identification of olivine formed after specific minerals in both our melting and

contamination experiments. Absolute values of textural features vary with experimental temperature and H_2O, where cluster density and 2D surface area tend to decrease, and grain boundary segment length increases with increasing temperature and H_2O content. How growth textures of peritectic olivine vary with parameters that were not varied in our experiments (e.g., pressure, heating or cooling rate) remains to be explored. We anticipate, however, that textural differences between peritectic olivine formed after different precursor minerals will propagate under varied conditions and in natural systems. For example, we suspect that olivine formed after phlogopite will always form fewer and smaller crystals than olivine formed after orthopyroxene, but absolute crystal sizes, GBS length, and cluster density will be a function of the crystallization conditions.

Peritectic olivine in TSP lavas

We interpret Type-1 olivine as peritectic crystals, because they form crystal clusters that resemble peritectic olivine produced in our melting experiments and previous contamination experiments (Erdmann *et al.*, 2010). We consider it unlikely that the Type-1 olivine is a magmatic glomerocryst, because magmatic olivine of the samples is <500 μm in size, and thus smaller than the larger crystals of the cluster. A xenocrystic origin is possible, but deformation textures typical for olivine xenocrysts in TSP lavas are lacking. For Type-2 olivine we propose a peritectic origin, because primary magmatic olivine is smaller and equant, and because Type-2 crystals show features interpreted as crystallized, exotic melt film pseudomorphs that contain re-grown orthopyroxene, phlogopite, and sodic feldspar (cf. Dungan & Davidson, 2004). Moreover, crystals do not exhibit strong deformation features as most inferred olivine xenocrysts in TSP

lavas. Moreover, amphibole, phlogopite, and orthopyroxene are common constituents in xenoliths of some TSP lavas (Costa *et al.*, 2002).

Besides its larger size, the following Type-1 olivine textures compare to those of Ol2b formed by decomposition of amphibole in our MN melting experiments: (i) 2D GBSs are short ($\leq$0.7 mm) and the frequency peak is narrow (~0.05-0.20 mm); (ii) 2D surface area shows a relatively narrow range ($\leq$1.3 mm^2) and frequency peak ($\leq$0.2 mm^2); and (iii) few inclusions. Type-2 olivine is also significantly larger than crystals in our experiments, but the following features resemble those of Ol2a and Ol2c replacing orthopyroxene in our LN and MN experiments: (i) long 2D GBSs ($\leq$1.2 mm) and a wide frequency peak (~0.15-0.40 mm); (ii) a wide range in 2D surface area ($\leq$2.5 mm^2); and (iii) common embayments and inclusions filled by crystallized melt. The pattern of 2D GBS length exhibits a low between ~0.20-0.25 mm. Together with the secondary peak at ~0.50 mm (twice the distance), we suspect that the low is an analytical artefact. The small number of crystals analyzed limits the significance of 2D surface area distribution, and scarcity of clusters complicates the interpretation. We nevertheless argue that, taken together, the textural features of Type-2 olivine point towards a formation after orthopyroxene. Both amphibole and orthopyroxene are common minerals in TSP country-rock contaminants (Costa et al., 2002), but rarely form xenocrysts (Dungan & Davidson, 2004).

The up to ~1000 and ~100 times larger crystal size of the natural olivine relative to the experimental crystals could partly reflect a larger grain size of the precursor crystals (i.e., crystals on the mm-scale rather than $\leq$170 μm as for our starting materials) and cotectic overgrowth. Textural coarsening by coalescence or Ostwald ripening may have consumed smaller cluster crystals at the expanse of larger ones (e.g., Cabane *et al.*, 2005; Schiavi *et al.*, 2009). The higher ratio of GBS length to 2D surface area for olivine in the TSP lavas (>0.3 for mean values) versus

values for experimental olivine (<0.05 for mean values) partly reflects that our textural analyses omitted small embayments in the natural crystals (Fig. 5f), but nevertheless points towards a reduction in surface area over time. Moreover, heating rate and/or maximum temperature and thus dissolution and nucleation rates of reactive minerals may have been lower than in our experiments, resulting in the formation of fewer large crystals. Peritectic crystals that formed in the TSP system – either within country rocks or in magmas – were likely heated more slowly than crystals in our experiments and temperatures may have been buffered closer to their stability fields. As a result, precursor minerals likely decomposed more slowly, resulting in the formation of larger crystals with longer GBS lengths.

Under dynamic conditions (unlike our static experiments) differences in decomposition rate of reactive minerals may also affect the dispersal of the newly crystallized peritectic crystals (Fig. 14a,b). Type-1 olivine is commonly grouped in clusters similar to those observed in our experiments, perhaps indicating that crystals are connect in 3D by synneusis or Ostwald ripening. Individual crystals may therefore be unlikely to be dispersed during magmatic flow. Alternatively, large olivine crystals that formed more slowly by orthopyroxene decomposition (Fig. 12d) may have been more easily dispersed by magmatic flow (Fig. 14b). During prolonged magma residence with cotectic growth on peritectic cores, features observed in our experiments and those identified for Type-1 and Type-2 olivine crystals may be more and more obscured (Fig. 14c). We expect that peritectic crystals formed after different minerals may nevertheless be inferred from zoning in slow-diffusing elements such as P in olivine (Fig. 14d). Oscillatory and patchy zoning in P have been imaged in olivine from basalts, andesites, and dacites (Milman-Barris *et al.*, 2008), but the investigated olivine crystals have not yet been analyzed for trace-element zoning.

CONCLUSIONS

Melting experiments of the type performed here are useful guides for identification and interpretation of peritectic crystals in igneous rocks. We have shown that clusters of peritectic olivine may form by decomposition of orthopyroxene, amphibole, and phlogopite, and that olivine formed after the three minerals has distinct crystal sizes, grain boundary segmentation, and cluster density. High-density peritectic crystal clusters with large individual crystals and long grain boundary segments form by decomposition of high-temperature minerals (e.g., orthopyroxene). Low-density peritectic crystal clusters with small individual crystals and short GBSs form by decomposition of low-temperature minerals (e.g., phlogopite). Host melt composition, and in particular concentrations of fast-diffusing components, affect cluster assemblages (e.g., amphibole may decompose olivine or olivine-plagioclase). Cluster density and 2D surface area of peritectic olivine tend to decrease, and grain boundary segment length increases with increasing experimental temperature and H_2O content and decreasing SiO_2 content. Using crystal textures, we interpret two olivine populations of basaltic-andesitic lavas of the MEMS of the TSP complex as peritectic crystals that likely formed by decomposition of orthopyroxene and amphibole, which are common minerals in TSP country-rock contaminants. Notably, the natural olivine crystals have significantly larger 2D surface area and GBS length than those of experimental olivine, which may reflect slower decomposition of reactive minerals in the TSP system. Further experimental investigations, including dynamic experiments, will be essential for characterizing formation and textures of peritectic crystals replacing a variety of reactive minerals at variable conditions.

ACKNOWLEDGEMENTS

REFERENCES

Amma-Miyasaka, M. & Nakagawa, M. (2002). Origin of anorthite and olivine megacrysts in island-arc tholeiites: petrological study of 1940 and 1962 ejecta from Miyake-Jima volcano, Izu-Mariana arc. *Journal of Volcanology and Geothermal Research* **117**, 263-283.

Beard, J. S., Ragland, P. C. & Crawford, M. L. (2005). Reactive bulk assimilation: A model for crust-mantle mixing in silicic magmas. *Geology* **33**, 681-684.

Bédard, J. H. & Hébert, R. (1998). Formation of chromitites by assimilation of crustal pyroxenites and gabbros into peridotitic intrusions: North Arm Mountain massif. Bay of Islands ophiolite, Newfoundland, Canada. *Journal of Geophysical Research* **103**, 5165-5184.

Bédard, J. H., Hébert, R., Berclaz, A. & Varfalvy, V. (2000). Syntexis and the genesis of lower oceanic crust. *Geological Society of America Special Paper* **349**, 105-119.

Behrens, H. & Gaillard, F. (2006). Geochemical aspects of melts; volatiles and redox behavior. *Elements* **2**, 275-280.

Brearley, M. & Scarfe, C. M. (1986). Dissolution rates of upper mantle minerals in an alkali basalt melt at high pressure: An experimental study and implications for ultramafic xenolith survival. *Journal of Petrology* **27**, 1137-1182.

Cabane, H., Laporte, D. & Provost, A. (2005). An experimental study of Ostwald ripening of olivine and plagioclase in silicate melts: implications for the growth and size of crystals in magmas. *Contributions to Mineralogy and Petrology* **150**, 37-53.

Clarke, D. B. (2007). Assimilation of xenocrysts in granitic magmas; principles, processes, proxies, and problems. *The Canadian Mineralogist* **45**, 5-30.

Coogan, L. A. (2003). Contaminating the lower crust in the Oman ophiolite. *Geology* **31**, 1065-1068.

Costa, F., Dungan, M. & Singer, B. (2002). Hornblende- and phlogopite-bearing gabbroic xenoliths from Volcan San Pedro (36°S), Chilean Andes: Evidence for melt and fluid migration and reactions in subduction-related plutons. *Journal of Petrology* **43**, 219–241.

Costa, F., Scaillet, B. & Pichavant, M. (2004). Petrologic and phase equilibria constraints on the pre-eruption conditions of Holocene dacite from Volcan San Pedro (36°S, Chilean Andes) and the importance of sulfur in silicic subduction-related magmas. *Journal of Petrology* **45**, 855–881.

Costa, F. & Dungan, M. (2005). Short time scales of magmatic assimilation from diffusion modeling of multiple elements in olivine. *Geology* **33**, 837-840.

Couch, S., Sparks, R. S. J. & Carroll, M. R. (2001). Mineral disequilibrium in lavas explained by convective self-mixing in open magma chambers. *Nature* **411**, 1037–1039.

Davidson, J., Turner, S., Handley, H., Macpherson, C. & Dosseto, A. (2007b). Amphibole "sponge" in arc crust? *Geology* **35**, 787–790.

Díaz-Alvarado J., Castro, A., Fernández, C. & Moreno-Ventas, I. (2011). Assessing bulk assimilation in cordierite-bearing granitoids from the Central System Batholith, Spain; experimental, geochemical and geochronological constraints. *Journal of Petrology* **52**, 223-256.

Dorais, M. J. & Tubrett, M. (2012). Detecting peritectic garnet in the peraluminous Cardigan Pluton, New Hampshire. *Journal of Petrology* **53**, 299-324.

Dungan, M. & Davidson, J. (2004). Partial assimilative recycling of the mafic plutonic roots of arc volcanoes: An example from the Chilean Andes. *Geology* **32**, 773–776.

Dungan, M. A., Wulff, A. & Thompson, R. (2001). Eruptive stratigraphy of the Tatara–San Pedro complex, 36°S, Southern volcanic zone, Chilean Andes: Reconstruction method and implications for magma evolution at longlived arc volcanic centers. *Journal of Petrology* **42**, 555–626.

Edwards, B. R. & Russell, J. K. (1996). A review and analysis of silicate mineral dissolution experiments in natural silicate melts. *Chemical Geology* **130**, 233-245.

Erdmann, S., Jamieson, R. A. & MacDonald, M. A. (2009). Evaluating the origin of garnet, cordierite, and biotite in granitic rocks: a case study from the South Mountain Batholith, Nova Scotia. *Journal of Petrology* **50**, 1477-1503.

Erdmann, S., Scaillet, B. & Kellett, D. A. (2010). Xenocryst assimilation and formation of peritectic crystal clusters during magma contamination: an experimental study. *Journal of Volcanology and Geothermal Research* **198**, 355-367.

France, L., Idefonse, B. & Koepke, J (2009). Interactions between magma and hydrothermal system in Oman ophiolite and in IODP Hole 1256D: Fossilization of a dynamic melt lens at fast spreading ridges. G^3, Q10O19, doi:10.1029/2009GC002652.

Johannes, W., Koepke, J., Behrens, H. (1994). Partial melting reactions of plagioclase and plagioclase-bearing systems. In: Parsons, I. (ed) *Feldspars and their reactions,* 161-194.

Lackey, J. S., Erdmann, S., Hark, J. S., Nowak, R. M., Clarke, D. B. & Valley, J. W. (2011). Tracing garnet origins in granitoids by oxygen isotope analysis: examples from the South Mountain Batholith, Nova Scotia. *The Canadian Mineralogist* **49**, 417-439.

Milman-Barris, M. S., Beckett, J. R., Baker, M. B., Hofmann, A. E., Morgan, Z., Crowley, M.R., Vielzeuf, D. & Stolper, E. (2008). Zoning of phosphorus in igneous olivine. *Contributions to Mineralogy and Petrology* **155**, 739-765.

O'Driscoll, B., Donaldson, C. H., Daly, S. & Emeleus, C. H. (2009). The roles of melt infiltration and cumulate assimilation in the formation of anorthosite and a Cr-spinel seam in the Rum Eastern Layered Intrusion, NW Scotland. *Lithos* **111**, 6-20.

Pownceby, M. I. & O'Neill, H. St. C. (1994). Thermodynamic data from redox reactions at high temperatures. III. Activity-composition relations in Ni-Pd alloys from EMF measurements at 850-1250 K, and calibration of the NiO + Ni-Pd assemblage as a redox sensor. *Contributions to Mineralogy and Petrology* **116**, 327-339.

Reubi, O. & Blundy, J. (2008). Assimilation of plutonic roots, formation of high-K 'exotic' melt inclusions and genesis of andesitic magmas at Volcán De Colima, Mexico. *Journal of Petrology* **49**, 2221-2243.

Scaillet, B., Pichavant, M. & Roux, J. (1995). Experimental crystallization of leucogranite magmas. *Journal of Petrology* **36**, 663-705.

Scaillet, B. & Evans, B. (1999). The 15 June 1991 eruption of Mount Pinatubo. I. Phase equilibria and pre-eruption $P–T–f$H$_2$O$–f$O$_2$ conditions of the dacite magma. *Journal of Petrology* **40**, 381–411.

Schiavi, F., Walte, N. & Keppler, H. (2009). First in-situ observation of crystallization processes in a basaltic andesite melt with moissanite cell. *Geology* **37**, 963-966.

Sisson, T. W. & Grove, T. L. (1993). Experimental investigation of the role of H$_2$O in calcalkaline differentiation and subduction zone magmatism. *Contributions to Mineralogy and Petrology* **113**, 143–166.

Stevens, G., Villaros, A. & Moyen, J.-F. (2007). Selective peritectic garnet entrainment as the origin of geochemical diversity in S-type granites. *Geology* **35**, 9-12.

Whitney, D. L. & Evans, B. W. (2010). Abbreviations for names of rock-forming minerals. *American Mineralogist* **95**, 185–187.

Zhang Y., Walker, D. & Lesher, C. E. (1989). Diffusive crystal dissolution. *Contributions to Mineralogy and Petrology* **102**, 492-513.

FIGURE CAPTIONS

Figure 1: Reactive assimilation and peritectic crystals. (a) Sketch depicting reactive assimilation of source-inherited solids during magma ascent (1), during magma mixing (2), magma self-mixing including erosion of wall-rock crystal mush (3), and country-rock assimilation (4). CR=country rocks; M1 and M2=two magma batches; CM=magmatic wall-rock crystal mush. (b) Sketch depicting progressive assimilation of a xenolith and experiments employed to study reactions and reaction products. Melting experiments (ME) mimic partial melting in a core zone, without compositional contribution from the host magma. Contamination experiments (CE; Erdmann *et al.*, 2010) simulate assimilation of xenoliths and xenocrysts in contact with host magmas or mixed melts of xenolith and host magma. In this study we present new results for two series of melting experiments. In the discussion we compare our melting experiments to earlier contamination experiments. (c) BSE image of an experimentally produced, "typical" peritectic clinopyroxene cluster (modified from Erdmann *et al.*, 2010).

Figure 2: (a) Leuconorite and (b) melanorite starting rocks. Experimental starting materials were rock powders of <170 μm or drilled rock cores ~8 mm long and ~4 mm in diameter. Ox=oxide; Id=iddingsite. All other mineral abbreviations follow Whitney and Evans (2010).

Figure 3: Summary of experimental run products and selected TSP olivines and their main characteristics. Mineral abbreviations follow those of Whitney & Evans (2010). Maximum dimension of restitic crystals is ~150 mm; peritectic crystals produced in experiments are shown to scale. BSE images of Type-1 and Type-2 olivine are 2.5 mm wide. * = Figure 4 gives more

details on textural characteristics of peritectic Ol1a to Ol1d. LN= leuconorite; MN = melanorite; exp. = experiment.

Figure 4: Subtypes of peritectic olivine in LN and MN melting experiments and their characteristic features. To classify and subsequently quantify textures the subtypes we pre-classified peritectic olivine according to cluster density, range in crystal size, and GBS length of large crystals. (a) Ol2a forms high-density clusters (~65 vol% Ol); large crystals have commonly long GBSs; some crystals have orthopyroxene (Opx) or glass (Gl) inclusions. (b) Ol2b forms medium-density clusters (~62 vol% Ol); GBSs of large crystals are short; inclusions are rare. (c) Ol2c forms high-density clusters (~68 vol% Ol); large crystals have commonly long GBSs; some crystals have orthopyroxene (Opx) or glass (Gl) inclusions. (d) Ol2d forms low-density clusters (~32 vol% Ol); small crystals are predominant; glass inclusions are absent.

Figure 5: Textural analysis of peritectic olivine. (a) BSE image of peritectic olivine in LN melting experiment. (b) For textural analyses, crystal outlines were manually traced. Grain boundary segments (GBSs) were measured as 2D length between inflection points of grain boundary outlines (marked by white diamonds). White line marks one GBS. (c) Cluster density was calculated as the 2D surface area of olivine crystals relative to the surface area of cluster glass. (d) Olivine of presumably peritectic origin in TSP lava. (e) Crystal outline traced for textural analysis showing one GBS (white line) and inflection points (white diamonds). Red arrows mark small-scale embayments and olivine-matrix intergrowths that were ignored for textural analysis. (f) Loose olivine cluster in TSP lava, presumably of peritectic origin.

Figure 6: Summary of starting material and run product modal proportions. Note that using rock powders caused some compositional/modal variation between experiments. (a) Assemblage of LN starting material. (b,c) Run products of LN partial melting in experiments with ~0.5 and ~2.3 wt% H_2O. (d) Assemblage of MN starting material. (e,f) Run products of MN partial melting with ~0.5 and ~2.3 wt% H_2O. Modal proportions of restitic crystals sharply decrease with increasing experimental temperature and H_2O. Modal proportions of recrystallized Pl1b and peritectic olivine first increase and then decrease with temperature.

Figure 7: BSE images of (a-c) leuconorite and (d-i) melanorite run products. Starting materials were rock powders (a,b,d-f) and rock cores (c,g-i). All scale bars are 100 μm. RCs=restitic crystals; PCs=peritectic crystals. Run conditions and modal assemblages of experiments are given in Table 3. Figure 3 shows a summary of all crystal types.

Figure 8: Composition of recrystallized plagioclase (Pl1b) and peritectic olivine rims, and glass. (a) Anorthite (An) of Pl1b is lower in LN and higher in MN experiments, and increases with experimental H_2O. (b) Forsterite (Fo) of Ol2 increases with experimental temperature in LN and MN experiments. (c,d) Trends in Al_2O_3 and CaO versus SiO_2 for LN and MN glasses. Glass produced in contamination experiments (data from Erdmann *et al.*, 2010) is relatively low in Al_2O_3 and CaO and high in SiO_2.

Figure 9: Textural data for Ol2a produced in LN melting experiments. Patterns of 2D surface area and 2D GBS length for LN-1 (a,b), LN-2 (c,d), and LN-8 (e,f). Grey dashed lines mark distribution of ≥70% of measurements around frequency peaks. Dashed black lines mark the

mean of GBS length. Note that Figures 8a,c,f show only part of the dataset; inset numbers indicate complete range. The 2D surface area decreases with increasing experimental temperature from LN-1 and LN-2 to LN-8. The 2D GBS length increases with experimental H_2O from LN-1 to LN-2, and with experimental temperature.

Figure 10: Textural data for Ol2b-d produced in melting experiment MN-8 performed at 1085 °C and 1.5 wt% H_2O. Data compares to measurements shown for LN-8 in Figure 9e,f. Patterns of 2D surface area and 2D GBS length for Ol2b (a,b), Ol2c (c,d), and Ol2d (e,f). Grey dashed lines mark distribution of ≥70% of measurements around frequency peaks. Dashed black lines mark the mean of GBS length. Note that Figure 10c shows only part of the dataset; inset number indicates complete range. The 2D surface area and GBS length increases from Ol2c to Ol2b and Ol2d. Notably, frequency peaks of Ol2c are broader (Fig. 10c,d) than for Ol2b (Fig. 10a,b) and Ol2d (Fig. 10e,f).

Figure 11: Textural data for Type-1 and Type-2 olivine from TSP lavas. (a) Cluster of Type-1 olivine. Arrows mark some oxide and plagioclase crystals. Composite BSE image. (b) Type-1 olivine GBS length is <0.7 mm with a narrow frequency peak at ~0.05-0.20 mm. (c) Type-1 olivine 2D surface area is predominantly <0.2 mm^2. Patterns of 2D GBS length and surface area compare to those of Ol2b (Fig. 10a,b). (d) Collage of Type-2 olivine crystals. Different grey levels reflect imaging conditions, not variable composition. Arrows mark main embayments and inclusions filled by matrix minerals and void space. (e) Type-2 olivine has GBS lengths <0.7 mm and a broad frequency peak at ~0.15-0.40 mm. (c) Type-2 olivine 2D surface area shows a large range, such as those of Ol2a (Fig. 9) and Ol2c (Fig. 10c,d).

Figure 12: Sketch illustrating crystals of the starting materials (a-d) and our interpretation of their reaction products (e-h). We infer that stability temperature (T) and rate of decomposition of reactive minerals, exerts important control on cluster density and size of peritectic crystals formed. High-temperature minerals, such as orthopyroxene in MN and LN experiments, that slowly decompose form high-density clusters with large crystals. Low-temperature minerals, such as amphibole and phlogopite in MN experiments, that rapidly decompose form low-density clusters and small crystals.

Figure 13: BSE images of contamination experiments C2 run at 1085 °C with 1.5 wt% H_2O (a-c; Erdmann *et al.*, 2010) and C4 run in parallel at 1085 °C with 2.5 wt% H_2O (d-i; Erdmann unpubl. data). In both experiments a partially crystallized basaltic andesite was contaminated by 25 wt% of the MN contaminant. (a) In C2 orthopyroxene forms sub-rounded xenocrysts. (b) Olivine commonly forms clusters with plagioclase (b,c), which we originally interpreted as the decomposition products of amphibole. Rare clusters of olivine-plagioclase-clinopyroxene were interpreted to have formed after amphibole and in a reaction with orthopyroxene. On the basis of our new textural data, we interpret olivine shown in the BSE images as the peritectic products of orthopyroxene (d); amphibole (b,e), and phlogopite (c,f). All images are to scale. XC=xenocryst; p=peritectic.

Figure 14: Inferred formation, dispersal, and cotectic growth of peritectic crystals in magma systems with increasing residence time (t1 → t4). (a) Peritectic olivine forms after amphibole and orthopyroxene. (b) Olivine formed after amphibole texturally anneals to anhedral crystals in 3D.

Olivine formed after orthopyroxene is larger and more easily dispersed by magmatic flow or gravity. (c) Cotectic overgrowths form. (d) Diffusive re-equilibration relaxes zoning patterns, particularly for fast-diffusing elements. Nevertheless, different types of compositional zoning may distinguish peritectic olivine formed after different reactive minerals.

Figure 1 - Erdmann et al.

Figure 2 - Erdmann et al.
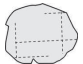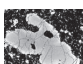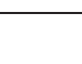
Phase		Crystal type	Main characteristics	Occurrence
Ol1		Restitic	Large, sub-rounded, normally or reversely zoned single crystals	MN exp.
Opx1		Restitic	Large, sub-rounded, unzoned single crystals	LN, MN exp.
Cpx1		Restitic	Large, sub-rounded, unzoned single crystals	LN exp.
Pl1a		Restitic	Large, sub-rounded, unzoned single crystals (An-poor)	LN, MN exp.
Pl1b		Recrystall.	Spongy-cellular, reversely zoned crystals (An-rich)	LN, MN exp.
Ox1		Restitic/ Recrystall.	Sub-rounded cores with spongy-cellular rims	LN, MN exp.
Ox2		Cotectic	Small, euhedral to skeletal crystals	MN exp.
Ol2a*		Peritectic	Cluster of large, subhedral to euhedral, unzoned crystals	LN exp.
Ol2b*		Peritectic	Cluster of small, subhedral to euhedral, unzoned crystals	MN exp.
Ol2c*		Peritectic	Cluster of large, subhedral to euhedral, unzoned crystals	MN exp.
Ol2d*		Peritectic	Cluster of small, subhedral to euhedral, unzoned crystals	MN exp.
Type-1		Peritectic?	Cluster of subhedral, normally zoned crystals	TSP lava
Type-2		Peritectic?	Cluster and subhedral single crystals with melt-film pseudomorphs	TSP lava

Figure 3 - Erdmann et al.

(a) LN

Ol2a

High-density cluster,
large crystals with long GBS,
some Opx and glass inclusions

(b) MN

Ol2b

Medium-density cluster,
large crystals with short GBS,
rare glass inclusions

(c) MN

Ol2c

High-density cluster,
large crystals with long GBS,
some Opx and glass inclusions

(d) MN

Ol2d

Low-density cluster,
small crystals, rare
Ox and glass inclusions

Opx/gl
incl.

Opx/gl
incl.

~65 vol% Ol

~60 vol% Ol

~68 vol% Ol

~32 vol% Ol

~50 um

Figure 4 - Erdmann et al.

Figure 5 - Erdmann et al.
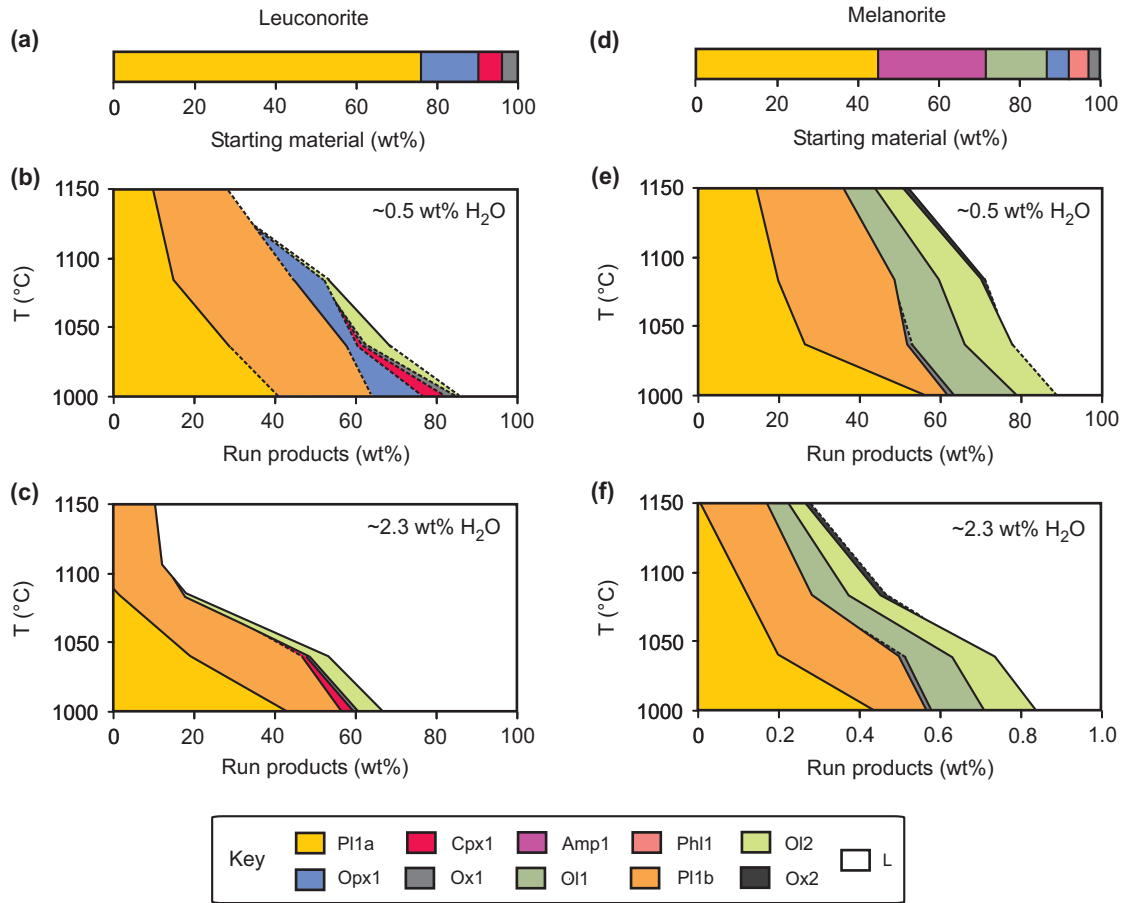
Figure 5 - Erdmann et al.

RCs - Ol1, Pl1a, Cpx1, Opx1, Ox1   RCCs - Pl1b, Ox1   PCs - Ol2a, Ol2b, Ol2c, Ol2d
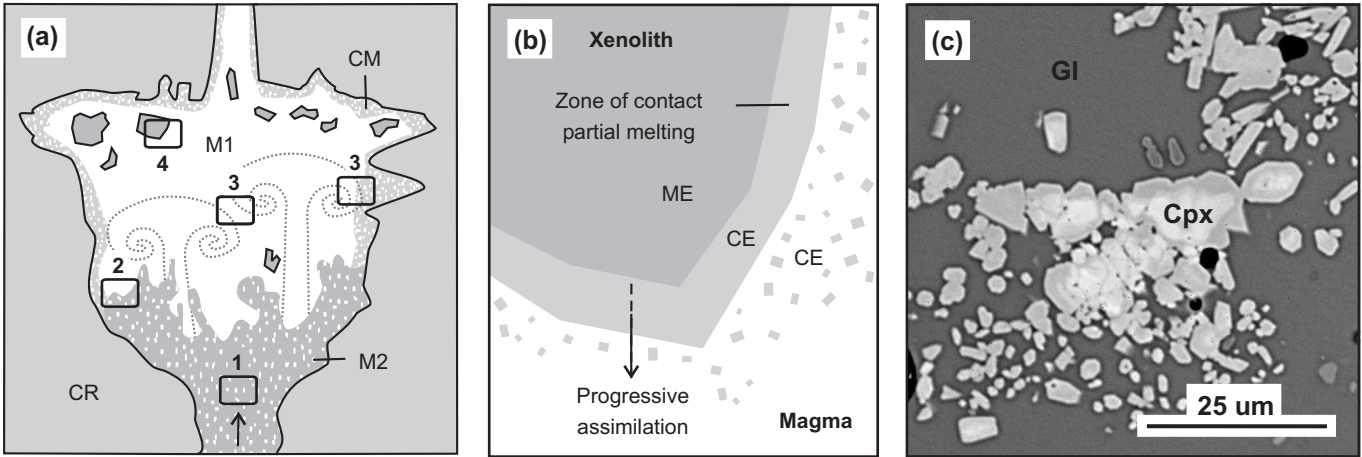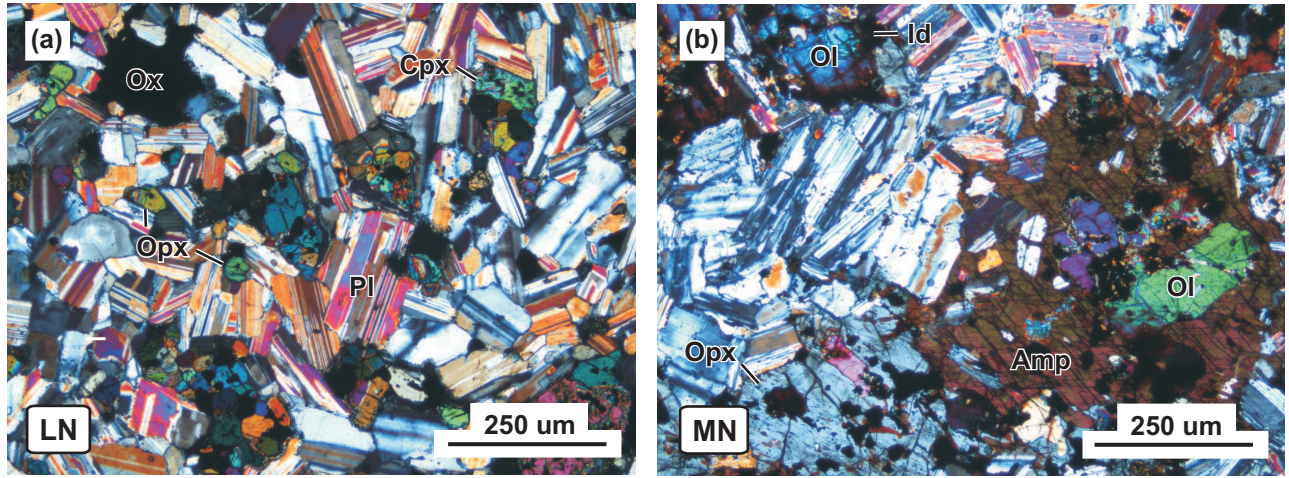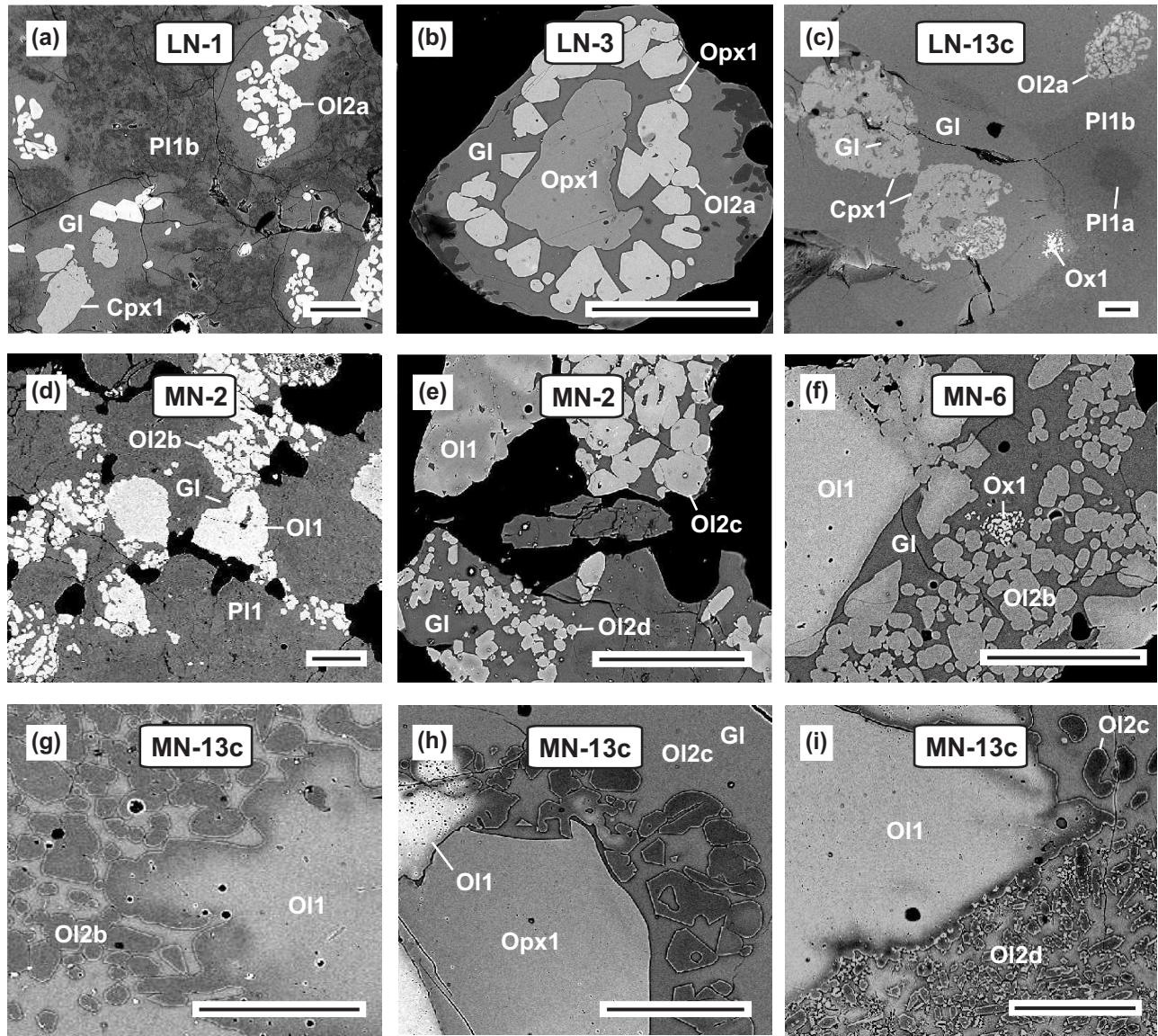

Figure 7 - Erdmann et al.
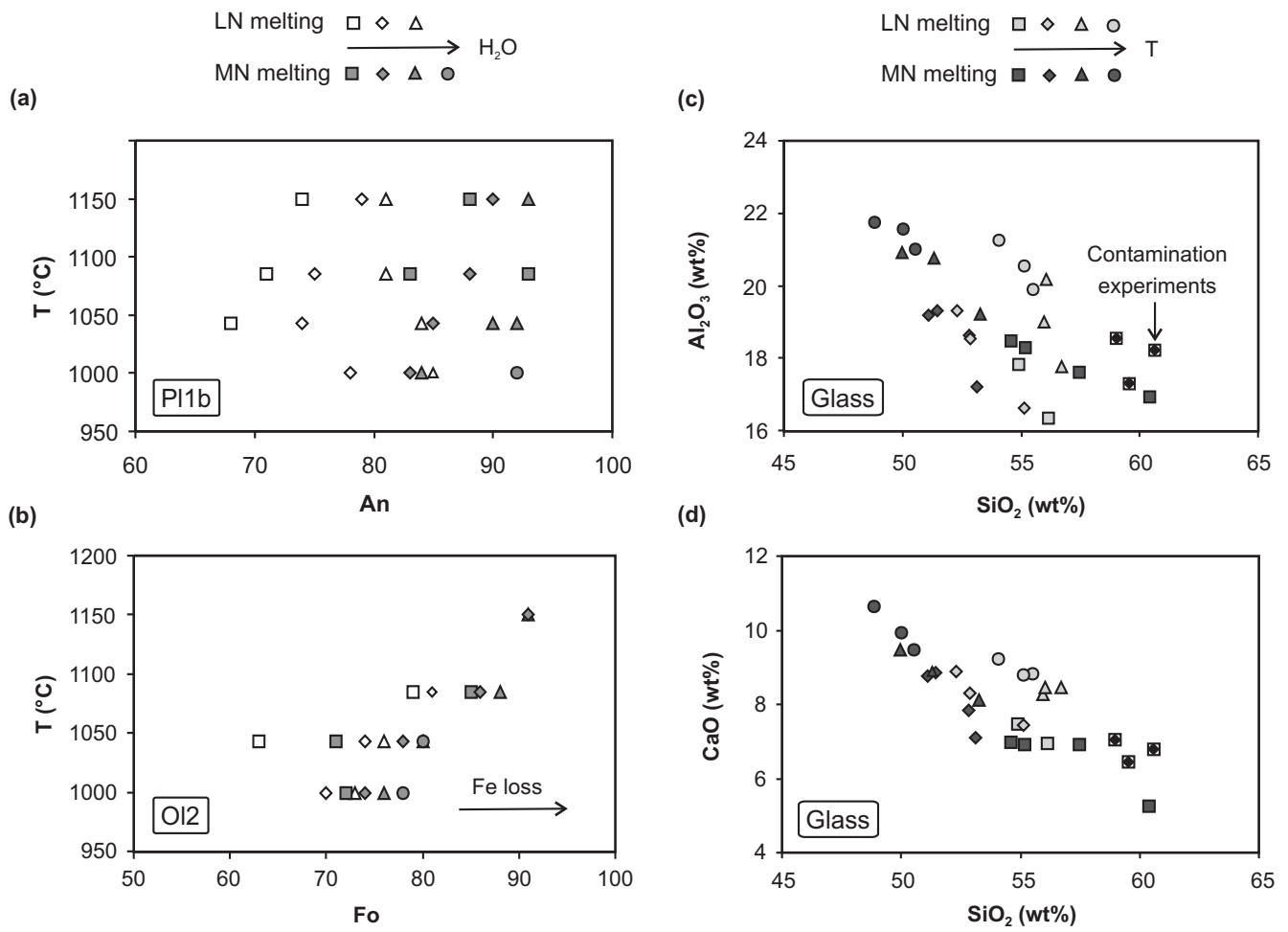
Figure 8 - Erdmann et al.
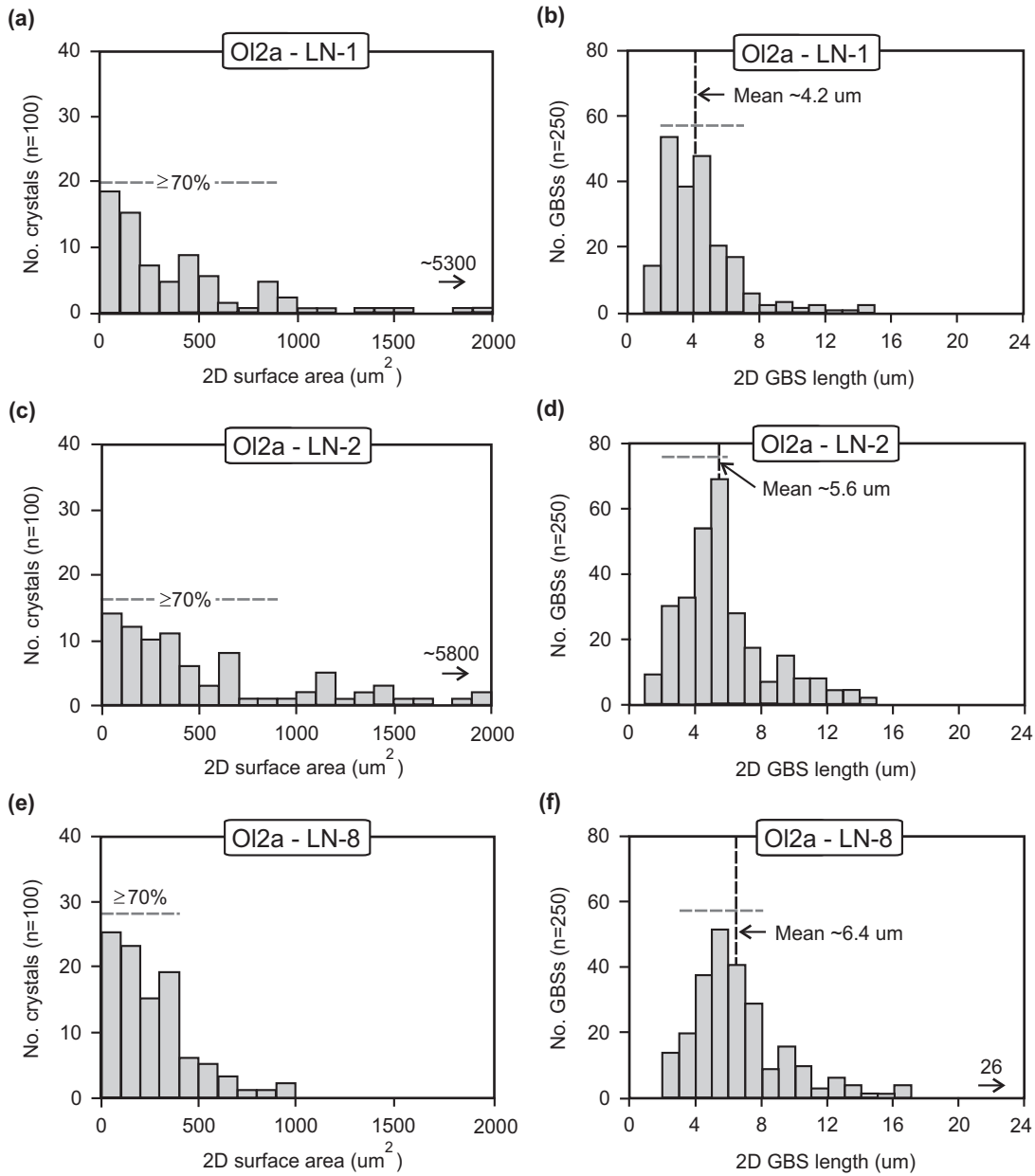
Figure 9 - Erdmann et al.
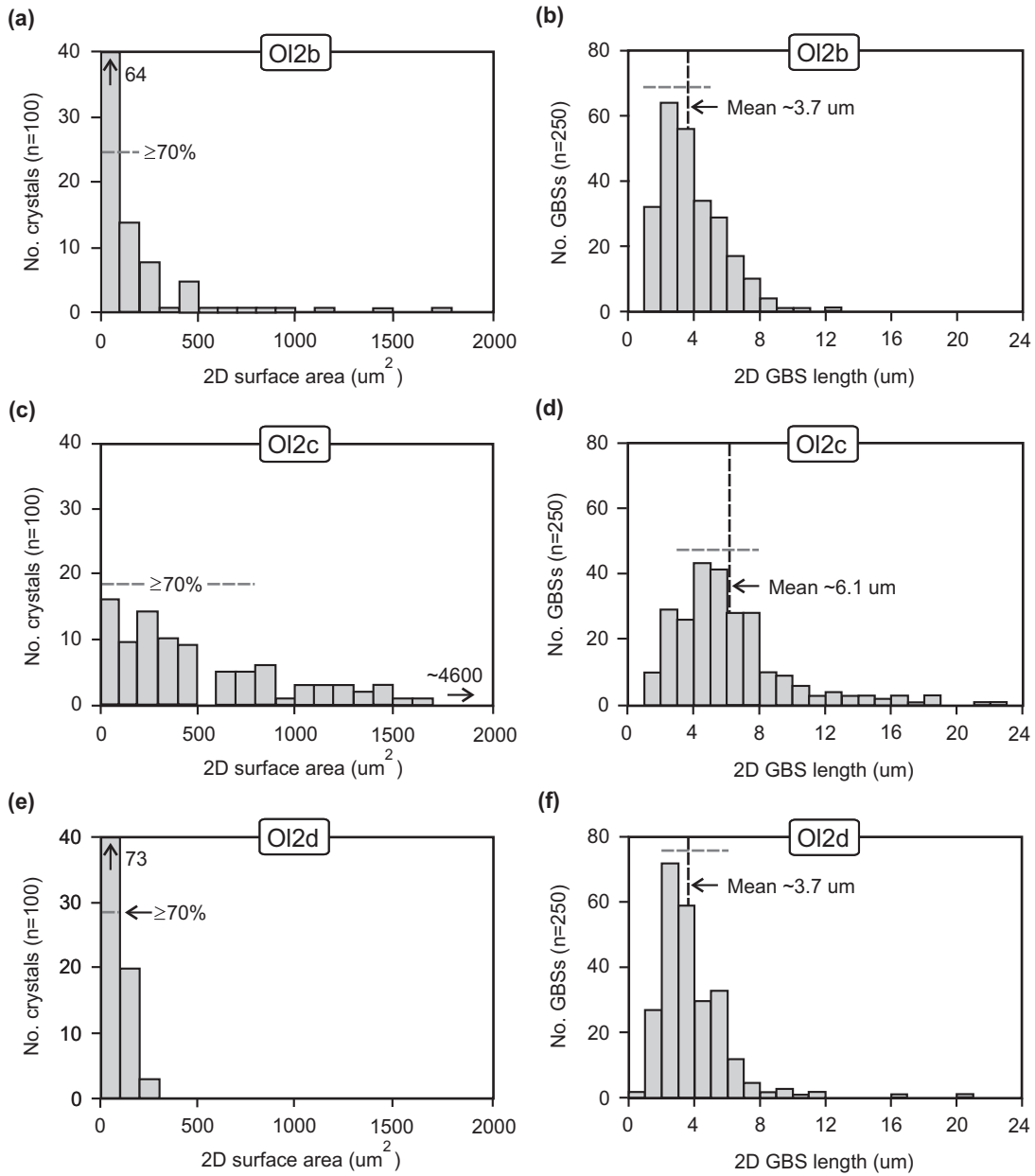
Figure 10 - Erdmann et al.
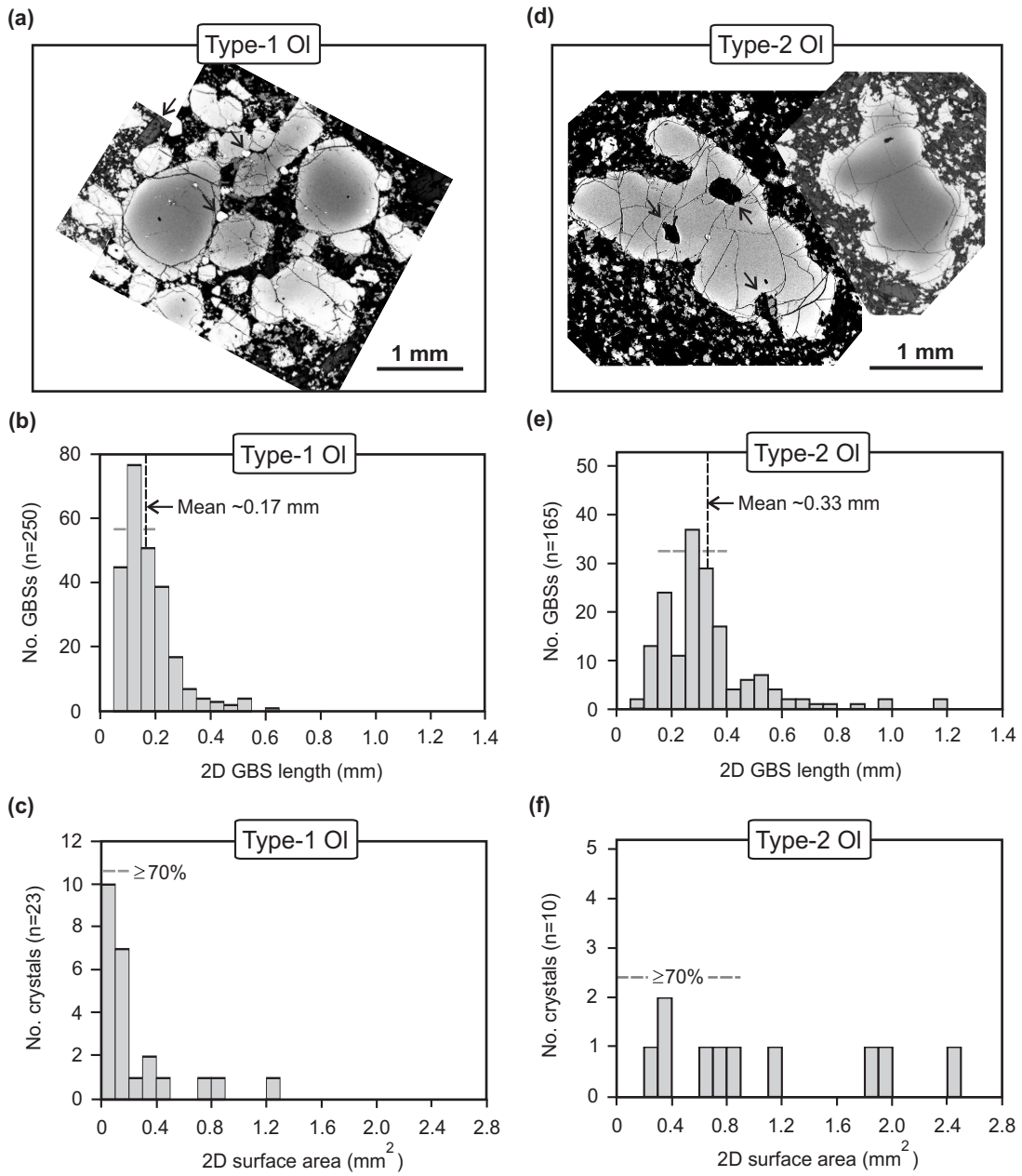
(a)

Type-1 Ol

1 mm

(d)

Type-2 Ol

1 mm

(b)

Type-1 Ol

No. GBSs (n=250)

Mean ~0.17 mm

2D GBS length (mm)

(e)

Type-2 Ol

No. GBSs (n=165)

Mean ~0.33 mm

2D GBS length (mm)

(c)

Type-1 Ol

No. crystals (n=23)

≥70%

2D surface area (mm^2)

(f)

Type-2 Ol

No. crystals (n=10)

≥70%

2D surface area (mm^2)

Figure 11 - Erdmann et al.

(a) Opx (MN)

$X_{Mg}\sim0.80$

(c) Opx (LN)

$X_{Mg}\sim0.66$

(e) Amp (MN)

$X_{Mg}\sim0.77$

(g) Phl (MN)

$X_{Mg}\sim0.80$

High ← Stability T of reactive mineral → Low

Low ← Decomposition rate → High

(b) Ol2c

(d) Ol2a

(f) Ol2b

(h) Ol2d

~50 um

~68 vol% Ol

~65 vol% Ol

~60 vol% Ol

~32 vol% Ol

Low ← Ol nucleation rate → High

Figure 12 - Erdmann et al.

(a) C2 — Ol2b, Pl1a, Pl2
~60% Ol
70% ≤160 um^2
Mean GBS 3.9 um

(b) C2 — Cpx2, Pl2, Ol2b?, Opx1
~46% Ol
70% ≤160 um^2
Mean GBS 4.0 um

(c) C2 — Ol1, Ol2d, Pl2
~34% Ol
70% ≤55 um^2
Mean GBS 3.7 um

(d) C4 — Ol2c
~63% Ol
70% ≤800 um^2
Mean GBS 6.6 um

(e) C4 — Ol2b
~62% Ol
70% ≤150 um^2
Mean GBS 3.8 um

(f) C4 — Ol2d
~31% Ol
70% ≤85 um^2
Mean GBS 3.7 um

50 um

Figure 13 - Erdmann et al.

(a) **t1: Beginning decomposition of crystals within xenoliths**

Amp

Opx
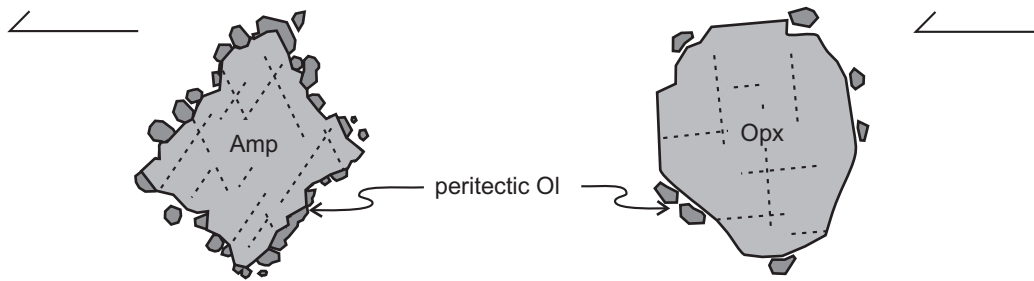
peritectic Ol

(b) **t2: Progressive formation of peritectic olivine ± dispersal in host melt**

coalscence of
Ol crytals

dispersal of
Ol crytals
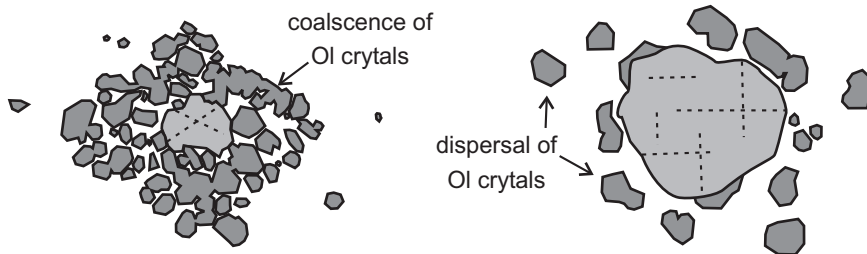
(c) **t3: Immersion in host magma, cotectic Ol overgrowths form**
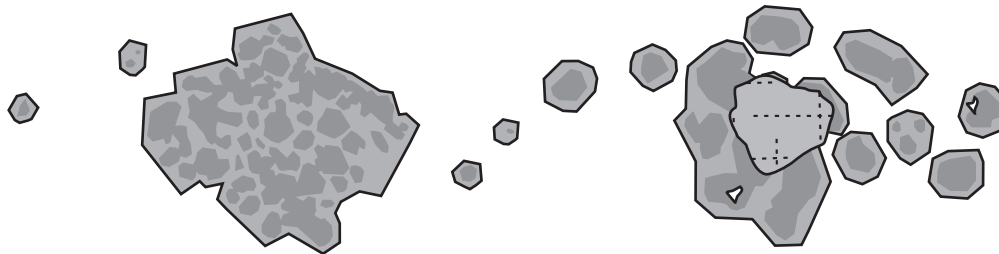
(d) **t4: Cotectic growth continues, zoning is modified by diffusive re-equilibration**

Fine patchy
zoning

Coarse patchy
zoning

~50 um
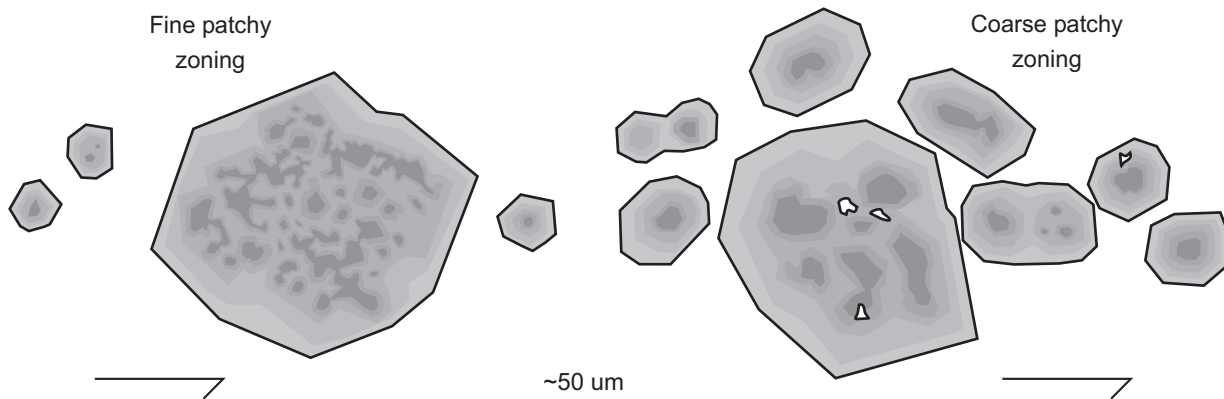
Figure 14 - Erdmann et al.

Table 1: Whole-rock geochemical composition and mineralogy of starting materials (in wt%)

St. Mat.	SiO_2	TiO_2	Al_2O_3	Fe_2O_3	MnO	MgO	CaO	Na_2O	K_2O	P_2O_5	Total
LN	52.13	0.64	22.26	6.21	0.11	3.91	9.88	3.75	0.28	0.08	99.24
MN[a]	45.69	0.44	22.29	7.76	0.11	10.73	10.56	2.11	0.46	0.07	100.22

St. Mat.	Ol[b]	Pl	Cpx	Opx	Amp	Phl	Ox
LN	-	76	6	14	-	-	4
MN[a]	15	45	-	5	27	5	3

St. Mat.=starting material; LN=leuconorite; MN=melanorite. Total Fe given as Fe_2O_3. Modal mineralogy estimated from thin sections and starting rock powders. a=data from Erdmann *et al.* (2010); b=Olivine is partly altered to iddingsite.

Table 2: Representative mineral compositions of starting materials

Material	MN[#]		MN[#]		MN[#]		MN[#]	
Mineral	Pl		Amp		Ol		Opx	
wt%	n=6	σ	n=5	σ	n=4	σ	n=3	σ
SiO_2	47.35	0.96	42.91	0.52	38.64	0.09	54.60	0.26
TiO_2	-	-	2.78	0.42	0.02	0.02	0.18	0.00
Al_2O_3	32.93	0.52	11.46	0.44	0.01	0.01	0.94	0.11
FeO	0.21	0.03	8.44	0.13	19.59	0.34	12.68	0.70
MnO	0.01	0.01	0.16	0.06	0.38	0.04	0.41	0.01
MgO	0.03	0.01	15.60	0.31	40.09	0.12	28.38	0.13
CaO	16.23	0.63	10.87	0.18	0.01	0.01	0.96	0.01
Na_2O	2.18	0.36	2.53	0.07	0.00	0.00	0.04	0.00
K_2O	0.04	0.02	0.52	0.05	0.02	0.02	0.02	0.02
BaO	0.00	0.01	-	-	-	-	-	-
NiO	-	-	0.03	0.03	0.12	0.01	0.05	0.01
Cr_2O_3	-	-	0.07	0.03	0.02	0.02	0.04	0.04
Total	98.96		95.36		98.89		98.29	
	An=80	3	X_{Mg}=77	1	Fo=78	<1	En=78	1
							Fs=20	1
							Wo=2	<1
							X_{Mg}=80	1

Material	MN[#]		LN		LN		LN	
Mineral	Phl		Pl		Cpx		Opx	
wt%	n=6	σ	n=6	σ	n=4	σ	n=4	σ
SiO_2	38.40	0.45	54.62	0.54	51.68	0.74	52.48	0.26
TiO_2	2.11	0.53	-	-	0.49	0.14	0.28	0.06
Al_2O_3	15.89	0.40	28.04	0.26	2.05	0.33	0.93	0.11
FeO	8.65	0.66	0.29	0.01	9.61	1.24	20.24	0.23
MnO	0.07	0.03	0.00	0.01	0.37	0.05	0.71	0.09
MgO	20.01	0.43	0.02	0.01	15.04	1.30	23.07	0.22
CaO	0.02	0.01	10.62	0.33	19.47	2.58	1.08	0.14
Na_2O	1.56	0.21	5.16	0.17	0.33	0.04	0.02	0.01
K_2O	7.64	0.36	0.29	0.02	-	-	-	-
BaO	0.24	0.08	0.02	0.02	-	-	-	-
NiO	0.10	0.03	-	-	0.01	0.02	0.02	0.01
Cr_2O_3	0.11	0.05	-	-	0.00	0.00	0.03	0.03
Total	94.80		99.06		99.05		98.86	
	X_{Mg}=80	1	An=53	2	En=44	4	En=65	<1
					Fs=16	2	Fs=33	1
					Wo=40	7	Wo=2	<1
					X_{Mg}=74	<1	X_{Mg}=66	1

Data are average concentrations (of n analyses) and standard deviation (σ). MN=melanorite;
LN=leuconorite; Fo=(Mg/(Mg+Fe)*100; An=(Ca/(Ca+Na+K)*100);
En=Mg/(Mg+Fe+Mn+Ca)*100); Fs=((Fe+Mn)/(Mg+Fe+Mn+Ca)*100);
Wo=Ca/(Mg+Fe+Mn+Ca)*100); X_{Mg}=(Mg/(Mg+Fe)*100).
# Data reported by Erdmann *et al.* , (2010)

Table 3: Experimental conditions and run products

Experiment	T	H$_2$O	t	ΔFeO	Phase proportions (wt%)								
	(°C)	(wt%)	(h)	%	Gl	Pl1a[a]	Pl1b[a]	Ol1[a]	Ol2[a]	Opx1	Cpx1	Ox1	Ox2
LN-1	1000	2.1	23	n.a.	34	42	14	0	7	0	3	<1	0
LN-2	1000	4.2	23	n.a.	50	30	13	0	5	0	2	0	0
LN-3	1043	0.5	25	n.a.	32	29	29	0	6	3	1	<1	0
LN-4	1043	2.1	25	n.a.	47	19	28	0	5	0	1	<1	0
LN-5	1043	4.2	25	n.a.	74	7	17	0	1	0	<1	<1	0
LN-6	1043	9.6	25	n.a.	100	0	0	0	0	0	0	0	0
LN-7	1085	0.5	24	-21	45	15	31	0	1	8	0	0	0
LN-8	1085	1.5	24	-27	71	14	14	0	1	0	0	0	0
LN-9	1085	2.5	24	-32	81	3	16	0	0	0	0	0	0
LN-10	1150	0.5	21	-63	71	12	17	0	0	0	0	0	0
LN-11	1150	1.5	21	-52	79	4	17	0	0	0	0	0	0
LN-12	1150	2.5	21	-43	88	1	11	0	0	0	0	0	0
LN-13c	1043	4.3	24	n.a.	Gl-Pl1a-Pl1b-Ol2-Cpx1-Ox1								
MN-1	1000	2.1	22	n.a.	16	43	14	13	13	0	0	<1	0
MN-2	1000	4.1	22	n.a.	17	39	17	14	14	0	0	<1	0
MN-3	1043	0.5	23	n.a.	23	26	26	13	12	0	0	<1	0
MN-4	1043	2.1	23	n.a.	27	20	30	12	11	0	0	<1	0
MN-5	1043	4.2	23	n.a.	40	12	28	11	9	0	0	<1	0
MN-6	1043	9.0	23	n.a.	43	4	33	10	9	0	0	<1	0
MN-7	1085	0.5	24	-30	30	20	29	11	10	0	0	0	<1
MN-8	1085	1.5	24	-29	42	12	28	10	9	0	0	0	<1
MN-9	1085	2.5	24	-23	53	3	28	9	8	<1	0	0	<1
MN-10	1150	0.5	21	-41	48	15	22	8	7	0	0	0	<1
MN-11	1150	1.3	21	-43	58	6	23	7	6	0	0	0	<1
MN-12	1150	2.5	21	-39	71	2	17	6	4	0	0	0	<1
MN-13c	1150	1.5	2	n.a.	Gl-Pl1a-Pl1b-Ol1-Ol2-Opx1-Ox1-Ox2								

Note that using rock powders caused some compositional/modal variation between experiments. a=Relative proportions of Pl1a versus Pl1b and Ol1 versus Ol2 were estimated from BSE images. Experiments LN-13c and MN-13c employed cores, all other experiments employed rock powders. Fe loss (ΔFeO) was calculated as 100×(FeOCharge−FeOSt.Mat.)/FeOSt.Mat., where FeOCharge is calculated from crystals and glass. Average Fe loss is -48% in experiments at 1150 °C and -27% in experiments at 1085 °C. Iron loss estimates for 1000 and 1043 °C experiments are not available, owing to large residuals and large uncertainties in mass-balance calculations. In crystallization experiments performed at equivalent conditions, average Fe loss in 1043 °C experiments was -13%.Table 4 summarizes the textural characteristics of the experimental run products.

Table 4: Composition of recrystallized plagioclase (Pl1b) produced in experiments (in wt%)

Experiment	LN-1	σ	LN-2	σ	LN-3	σ	LN-4	σ	LN-5	σ	LN-7	σ	LN-8	σ	LN-9	σ
T (°C)	1000		1000		1043		1043		1043		1085		1085		1085	
H_2O	2.1		4.2		0.5		2.1		4.2		0.5		1.5		2.5	
n	2	σ	3	σ	3	σ	2	σ	8	σ	3	σ	3	σ	5	σ
SiO_2	48.43	0.04	46.54	0.34	50.55	0.54	49.03	0.07	46.88	0.60	49.67	0.61	49.66	0.56	47.18	1.25
Al_2O_3	30.74	1.01	32.30	1.27	30.85	0.26	31.56	0.06	33.67	0.67	31.64	0.47	31.81	0.08	33.65	2.08
$FeO^{\#}$	0.38	0.03	0.32	0.12	0.33	0.03	0.66	0.00	0.65	0.13	0.32	0.07	0.46	0.15	0.36	0.81
MgO	0.24	0.06	0.11	0.11	0.01	0.01	0.15	0.01	0.14	0.14	0.16	0.07	0.31	0.17	0.16	0.71
CaO	15.64	0.41	17.04	0.11	13.90	0.33	14.59	0.05	16.89	0.37	14.65	0.40	15.03	0.36	16.70	1.41
Na_2O	2.50	0.06	1.75	0.03	3.57	0.17	2.90	0.06	1.82	0.17	3.32	0.20	3.08	0.26	2.16	0.51
K_2O	0.09	0.04	0.02	0.00	0.15	0.02	0.06	0.01	0.05	0.02	0.06	0.01	0.06	0.01	0.04	0.01
Total	98.0	1.4	98.1	0.7	99.4	0.3	99.0	0.0	100.1	0.5	99.8	0.8	100.4	0.3	100.3	0.4
An	78	1	85	1	68	2	74	0	84	2	71	2	75	2	81	5

Experiment	LN-10	σ	LN-11	σ	LN-12	σ	MN-1	σ	MN-2	σ	MN-4	σ	MN-5	σ	MN-6	σ
T (°C)	1150		1150		1150		1000		1000		1043		1043		1043	
H_2O	0.5		1.5		2.5		2.1		4.1		2.1		4.2		9	
n	4	σ	4	σ	4	σ	4	σ	2	σ	3	σ	3	σ	4	σ
SiO_2	48.90	0.22	47.63	0.85	46.99	1.25	46.59	0.49	46.12	0.39	46.12	0.39	44.81	0.93	44.24	0.34
Al_2O_3	32.21	0.03	32.53	1.38	32.95	2.08	33.46	0.45	33.63	0.27	33.63	0.27	34.85	0.55	35.26	0.29
$FeO^{\#}$	0.28	0.07	0.45	0.26	0.75	0.81	0.37	0.12	0.36	0.03	0.36	0.03	0.42	0.11	0.52	0.03
MgO	0.13	0.07	0.48	0.42	0.55	0.71	0.02	0.01	0.02	0.01	0.02	0.01	0.07	0.03	0.10	0.04
CaO	14.99	0.19	15.79	0.90	16.29	1.41	16.61	0.41	16.88	0.26	16.88	0.26	18.23	0.64	18.60	0.37
Na_2O	2.97	0.10	2.29	0.32	2.05	0.51	1.84	0.16	1.69	0.16	1.69	0.16	1.14	0.34	0.88	0.14
K_2O	0.08	0.03	0.05	0.03	0.04	0.01	0.05	0.03	0.03	0.02	0.03	0.02	0.04	0.01	0.05	0.01
Total	99.6	0.1	99.2	0.7	99.6	0.4	99.0	0.3	98.7	0.2	98.7	0.2	99.6	0.1	99.7	0.2
An	74	1	79	3	81	5	83	2	84	1	85	1	90	3	92	1

Experiment	MN-7	σ	MN-8	σ	MN-9	σ	MN-10	σ	MN-11	σ	MN-12	σ
T (°C)	1085		1085		1085		1150		1150		1150	
H_2O	0.5		1.5		2.5		0.5		1.5		2.5	
n	3	σ	3	σ	4	σ	3	σ	4	σ	2	σ
SiO_2	45.11	0.02	43.64	0.56	43.68	0.36	44.65	0.25	44.64	0.76	44.14	0.09
Al_2O_3	35.12	0.05	35.49	0.49	36.58	0.20	34.99	0.45	35.15	0.48	35.31	0.26
$FeO^{\#}$	0.37	0.03	0.41	0.10	0.36	0.02	0.29	0.08	0.24	0.06	0.24	0.02
MgO	0.04	0.00	0.11	0.06	0.05	0.03	0.10	0.05	0.18	0.07	0.13	0.01
CaO	16.86	0.09	17.59	0.67	18.45	0.12	17.79	0.51	18.32	0.63	18.92	0.11
Na_2O	1.85	0.00	1.30	0.37	0.82	0.08	1.32	0.30	1.07	0.27	0.79	0.02
K_2O	0.05	0.01	0.06	0.00	0.05	0.01	0.06	0.02	0.06	0.02	0.04	0.00
Total	99.4	0.1	98.6	0.4	100.0	0.4	99.2	0.5	99.7	0.6	99.6	0.2
An	83	1	88	3	93	1	88	3	90	2	93	<1

Data are average concentrations of n analyses and standard deviation (σ). [#] Total Fe given as FeO.

Table 5: Textural data for peritectic olivine produced in experiments

Sample	LN-1	LN-2	LN-8	LN-8	LN-8	LN-8	LN-8	LN-8	LN-8
T (°C)	1000	1000	1085	1085	1085	1085	1085	1085	1085
H_2O	2.1	4.2	1.5	1.5	1.5	1.5	1.5	1.5	1.5
Olivine	Ol2a	Ol2a	Ol2a	Ol2a	Ol2a	Ol2a	Ol2a	Ol2a	Ol2a
No. clusters analyzed	3	4	6	C1	C2	C3	C4	C5	C6
Cluster density (%)	81	70	65	60	64	63	66	67	70
2D surface area	in um^2								
n	100	100	100	25	13	17	9	22	14
Mode	<100	<100	<100	<100	<100	<100	<100	<100	<100
Mean	563	914	264	259	248	262	264	247	293
Minimum	14	14	15	16	25	30	15	27	53
Maximum	5324	5784	927	921	640	865	913	640	666
σ	790	1103	202	218	190	212	250	170	158
$\overline{d}$	158	221	40	87	105	103	167	72	84
2D GBS length	in um								
n	250	250	250	50	50	50	50	50	50
Mode	2.5	5.5	5.5	5.5	5.5	6.5	6.5	5.5	5.5
Mean	4.2	5.6	6.4	6.5	6.2	7.3	6.9	8.0	6.4
Minimum	1.0	1.0	2.0	3.0	2.5	2.0	2.5	2.0	2.5
Maximum	15	15	26	15	12	17	26	26	12
σ	2.4	2.9	3.1	2.6	2.2	3.9	4.5	5.1	2.3
$\overline{d}$	0.3	0.4	0.4	0.7	0.6	1.1	1.3	1.4	0.6

Sample	MN-8	MN-8	MN-8	TSP	TSP
T (°C)	1085	1085	1085	-	-
H_2O	1.5	1.5	1.5	-	-
Olivine	Ol2b	Ol2c	Ol2d	Type-1	Type-2
No. clusters analyzed	6	3	3	1	10[a]
Cluster density (%)	60	68	32	<70	-
2D surface area	in um^2			in mm^2	
n	100	100	100	23	10
Mode	<100	<100	<100	<0.1	n.d.
Mean	171	774	81	0.25	1.05
Minimum	5	20	8	0.02	0.24
Maximum	1740	4556	424	1.22	2.44
σ	283	788	64	0.30	0.73
$\overline{d}$	57	158	13	0	0
2D GBS length	in um			in mm	
n	250	250	250	250	250
Mode	2.5	4.5	2.5	0.18	0.28
Mean	3.7	6.1	3.7	0.17	0.33
Minimum	1.0	1.0	0.5	0.05	0.06
Maximum	13	23	21	0.62	1.12
σ	1.0	3.8	2.2	0.10	0.18
$\overline{d}$	0.1	0.5	0.3	0.01	0.02

Data are average concentrations of n analyses. a=single crystals were analyzed. σ = standard deviation; $\overline{d}$ = standard error, equal to $2*\sigma/n^{1/2}$

Table 7: Composition of experimental glass (normalized to 100 wt% anhydrous)

Experiment	LN-1	σ	LN-2	σ	LN-3	σ	LN-4	σ	LN-5	σ	LN-6	σ	LN-7	σ
T (°C)	1000		1000		1043		1043		1043		1043		1085	
H_2O	2.1		4.2		0.5		2.1		4.2		9.6		0.5	
n	5		5		12		9		9		10		6	
SiO_2	56.15	0.33	54.89	0.59	55.63	0.76	55.12	0.74	52.86	0.38	52.29	0.26	55.89	0.57
TiO_2	1.67	0.15	1.22	0.15	2.00	0.33	1.60	0.20	1.05	0.17	0.96	0.13	1.46	0.14
Al_2O_3	17.43	0.16	19.00	0.11	15.95	0.20	17.17	0.26	19.28	0.18	20.15	0.20	18.26	0.10
$FeO^{\#}$	9.19	0.12	8.22	0.12	10.45	0.37	9.41	0.60	8.49	0.15	7.53	0.20	5.97	0.37
MnO	0.20	0.04	0.15	0.05	0.24	0.06	0.24	0.07	0.21	0.04	0.18	0.06	0.15	0.01
MgO	3.17	0.07	3.78	0.08	3.51	0.16	3.83	0.07	4.76	0.08	5.11	0.11	4.90	0.09
CaO	7.38	0.10	7.94	0.18	7.51	0.16	7.65	0.09	8.60	0.22	9.25	0.21	8.66	0.07
Na_2O*	4.41	0.14	4.46	0.07	4.20	0.21	4.63	0.18	4.51	0.18	4.30	0.15	4.18	0.09
K_2O	0.41	0.04	0.33	0.03	0.51	0.04	0.35	0.03	0.25	0.03	0.23	0.03	0.52	0.03
Total**	93.9		93.8		96.6		96.8		96.2		95.8		97.3	
X_{Mg}	38		45		37		42		50		55		59	
X_{Ca}	47		48		48		47		50		53		51	
Fe/Mg$_{Ol2-Gl}$	0.27		0.31		0.34		0.26		0.31		-		0.39	
Ca/Na$_{Pl1*-Gl}$	3.74		5.46		2.18		3.04		4.87		-		2.13	

Experiment	LN-8	σ	LN-9	σ	LN-10	σ	LN-11	σ	LN-12	σ	MN-1	σ	MN-2	σ
T (°C)	1085		1085		1150		1150		1150		1000		1000	
H_2O	1.5		2.5		0.5		1.5		2.5		2.1		4.2	
n	6		4		5		5		5		5		7	
SiO_2	55.12	0.17	55.06	0.15	55.49	0.27	55.11	0.19	54.07	0.07	57.45	0.14	55.18	0.27
TiO_2	1.01	0.05	0.90	0.02	0.98	0.02	0.90	0.05	0.79	0.03	1.36	0.14	1.15	0.12
Al_2O_3	19.53	0.05	20.75	0.07	20.34	0.14	21.08	0.11	21.91	0.08	18.50	0.09	19.28	0.11
$FeO^{\#}$	5.55	0.07	4.69	0.38	2.91	0.03	3.41	0.18	3.65	0.08	6.41	0.11	8.36	0.29
MnO	0.14	0.01	0.10	0.01	0.10	0.01	0.09	0.01	0.10	0.01	0.12	0.04	0.15	0.05
MgO	5.11	0.05	4.79	0.07	5.68	0.17	4.99	0.08	4.53	0.06	3.29	0.18	3.36	0.17
CaO	8.46	0.04	8.69	0.06	9.01	0.09	8.98	0.05	9.48	0.04	7.24	0.24	7.24	0.16
Na_2O*	4.64	0.07	4.64	0.05	5.10	0.08	5.09	0.06	5.15	0.07	4.07	0.09	3.96	0.16
K_2O	0.44	0.01	0.39	0.02	0.38	0.03	0.35	0.01	0.32	0.01	1.54	0.07	1.31	0.10
Total**	97.3		97.2		97.7		97.5		97.0		95.2		94.9	
X_{Mg}	62		65		78		72		69		48		42	
X_{Ca}	49		50		48		48		49		44		45	
Fe/Mg$_{Ol2-Gl}$	0.39		-		-		-		-		0.32		0.23	
Ca/Na$_{Pl1*-Gl}$	2.68		4.12		2.86		3.91		4.32		5.07		5.46	

Experiment	MN-3	σ	MN-4	σ	MN-5	σ	MN-6	σ	MN-7	σ	MN-8	σ	MN-9	σ
T (°C)	1043		1043		1043		1043		1085		1085		1085	
H_2O	0.5		2.1		4.2		9		0.5		1.5		2.5	
n	9		10		15		16		5		5		6	
SiO_2	53.13	1.28	52.81	0.63	51.07	0.72	51.43	0.45	53.35	0.26	51.35	0.33	49.96	0.08
TiO_2	1.34	0.12	0.75	0.08	0.62	0.11	0.52	0.10	1.26	0.03	0.86	0.03	0.64	0.02
Al_2O_3	18.15	0.39	19.88	0.28	20.53	0.29	20.77	0.38	19.99	0.18	21.58	0.13	21.92	0.10
$FeO^{\#}$	10.43	0.82	7.97	0.46	8.28	0.60	7.65	0.60	5.81	0.08	4.98	0.36	5.58	0.07
MnO	0.19	0.04	0.11	0.06	0.16	0.04	0.17	0.05	0.13	0.01	0.12	0.01	0.12	0.01
MgO	4.36	0.59	5.47	0.08	5.84	0.20	5.81	0.52	5.06	0.35	6.37	0.07	6.70	0.03
CaO	7.45	0.21	8.35	0.21	9.34	0.15	9.49	0.24	8.39	0.13	9.19	0.14	9.93	0.09
Na_2O*	3.59	0.14	3.73	0.14	3.42	0.20	3.54	0.25	4.34	0.09	4.39	0.12	4.14	0.08
K_2O	1.36	0.07	0.93	0.08	0.75	0.05	0.62	0.04	1.68	0.05	1.21	0.05	1.00	0.03
Total**	94.8		93.6		93.5		93.0		96.2		95.9		95.4	
X_{Mg}	43		55		56		58		61		70		68	
X_{Ca}	48		52		57		57		46		49		53	
Fe/Mg$_{Ol2-Gl}$	0.31		0.34		0.32		0.34		0.28		0.37		0.34	
Ca/Na$_{Pl1*-Gl}$	-		7.17		7.77		9.38		4.72		6.46		9.36	

Table 7: Continued

Experiment	MN-10		MN-11		MN-12	
T (°C)	1150		1150		1150	
H_2O	0.5		1.5		2.5	
n	7	σ	6	σ	7	σ
SiO_2	50.23	0.45	49.58	0.28	48.29	0.19
TiO_2	0.72	0.03	0.61	0.03	0.45	0.02
Al_2O_3	21.59	0.23	22.12	0.11	22.27	0.08
$FeO^{\#}$	4.39	0.10	3.92	0.13	4.18	0.05
MnO	0.10	0.01	0.08	0.00	0.08	0.01
MgO	7.99	0.29	8.45	0.09	8.97	0.04
CaO	9.71	0.16	10.18	0.09	10.88	0.06
Na_2O^*	4.22	0.15	4.17	0.06	4.20	0.07
K_2O	1.00	0.04	0.86	0.03	0.66	0.02
Total**	97.3		97.5		97.7	
X_{Mg}	76		79		79	
X_{Ca}	55		59		63	
Fe/Mg_{Ol2-Gl}	0.32		0.39		0.36	
Ca/Na_{Pl1^*-Gl}	5.09		5.67		6.93	

Data are average concentrations of n analyses and standard deviation (s). [#] Total Fe given as FeO. * Corrected relative to glass standards of Scaillet & Evans (1999). ** Pre-normalized analytical totals. Note that Fe/Mg and Ca/Na partition coefficients for olivine and plagioclase, respectively, are disequilibrium values. They do not represent the bulk systems, are affected by experimental Fe loss, and likely reflect only local and temporary equilibrium.